11-19-2021

Development of a near-infrared fluorescent daratumumab-based drug conjugate for targeted imaging and therapy in preclinical multiple myeloma

Nicholas Cho
Washington University in St. Louis

WASHINGTON UNIVERSITY IN ST. LOUIS

School of Engineering and Applied Sciences

Department of Biomedical Engineering

Dissertation Examination Committee:
Monica Shokeen, Chair
Samuel Achilefu
Gwendalyn Randolph
Michael Rettig
Quing Zhu

Development of a Near-infrared Fluorescent Daratumumab-based Drug Conjugate for Targeted Imaging and Therapy in Preclinical Multiple Myeloma

by

Nicholas Cho

A dissertation presented to
The Graduate School
of Washington University in
partial fulfillment of the
requirements for the degree
of Doctor of Philosophy

December 2021
Saint Louis, Missouri

Table of Contents

List of Figures

List of Tables

Acknowledgments

Dr. Monica Shokeen provided exceptional mentorship and support over the course of my doctoral research. Her knowledge of the field and limitless energy were an inspiration to me and helped me push the boundaries in my work. The intellectual freedom Dr. Shokeen provided during my graduate career transformed my outlook in research, and made me a better scientist that is unafraid to explore and ask the big questions of the field. I thank her for providing me with intellectually challenging and rewarding research questions and for building a rigorous foundation to my scientific education.

I would like to thank my colleagues in the Shokeen Lab for their continual support, in both personal and scientific pursuits. Dr. Anchal Ghai, Dr. Deep Hathi, and Sooah Ko in the Shokeen Lab have supported me in all my projects and were a source of inspiration for me for their unstinting work ethic, leadership, and ability to develop ideas into innovative research directions. Dr. Hathi has assisted me in several of my projects, particularly with animal handling and imaging, tissue culture experiments, and data analysis and presentation. I have greatly valued both his intellectual and professional support as well as his friendship during my graduate career and look forward to continuing our friendship in San Francisco.

Dr. Samuel Achilefu has been an excellent and endless source of advice and inspiration throughout my graduate education. He has provided creative solutions and continually challenged me to explore and integrate lateral thinking into my doctoral research. His guidance and mentorship, particularly during my time with Spectra, have helped foster my scientific growth and helped me become an independent scientist.

I would like to thank the members of the Optical Radiology Laboratory for their constant intellectual and emotional support and for always being there when I needed them. Thank you to

Dr. Christine O'Brien, Dr. Suman Mondal, Dr. Daniel Lane, Dr. Jessica Miller, Dr. Lemoyne Habimana-Griffin, Elizabeth Delassus, Katie Duncan, Megan Michie and many others for making the lab a better place and helping me grow as a person. Thank you to Dr. Kalen Dionne and Matt Mixdorf for their support inside and outside of the lab when I experienced my seizure in 2020 and helping me still make progress on my thesis.

I am grateful to my external collaborators Dr. Julie O'Neal and Dr. Francesca Fontana for teaching me the technical skills I needed to succeed in my research. Dr. O'Neal provided initial impetus in driving my first aim and provided valuable insights about flow cytometry and multiple myeloma. Dr. O'Neal and Dr. Fontana provided mentorship and training during my early years in the doctoral program, and especially helped me learn critical animal handling skills. Their expertise and enthusiasm were inspiring and assisted me in developing independence as a researcher.

My friends have provided me with endless support that has been critical for maintaining constant excellence and a positive attitude through all stages of my graduate education. I would especially like to thank Dr. Ian Berke, Dr. Amanda Dicks, Dr. Andy Daniel, Amrita Nishtala, Edward Hsieh, Michael Saad and many others for providing me with timely advice on navigating research and in helping fuel my personal and scientific growth over the years.

I would like to thank my family for their continued patience and support for me throughout my education and beyond. My parents have helped me work through difficult times in my PhD education and have remained a continual source of inspiration and advice.

Finally, I would like to acknowledge funding from the National Cancer Institute (NCI) grants R01 CA176221 and U54 CA199092. The support from the Imaging Sciences Pathway Fellowship [T32 EB014855] was also instrumental in my technical and professional

development during graduate school. Support was also provided from the National Institutes of Health (NIH) CA094056, DE-SC0012737, K08CA154790, and pilot imaging funds from the Mallinckrodt Institute of Radiology at the Washington University School of Medicine.

Nicholas Cho

Washington University in St. Louis

December 2021

ABSTRACT OF THE DISSERTATION

Development of a Near-infrared Fluorescent Daratumumab-based Drug Conjugate for Targeted Imaging and Therapy in Preclinical Multiple Myeloma

by

Nicholas Cho

Doctor of Philosophy in Biomedical Engineering

Washington University in St. Louis, 2021

Professor Monica Shokeen, Chair

Multiple myeloma (MM) is a debilitating hematologic malignancy of terminally differentiated plasma cells in the bone marrow (BM). Daratumumab (DARA) is an FDA-approved high-affinity monoclonal antibody targeting CD38 that has shown promising therapeutic efficacy in relapsed and refractory MM. Despite the well-established clinical efficacy of DARA, not all heavily pretreated patients respond to DARA monotherapy, and the majority of patients who initially respond eventually progress. This may be due to upregulation of pathways that inhibit DARA-mediated tumor killing. Antibody drug conjugates (ADCs) combine the highly targeted tumor antigen recognition of antibodies with cell killing properties of chemotherapy for effective internalization and processing of the drug. Here, we evaluated the antitumor efficacy of DARA conjugated to the maytansine derivative, mertansine (DM1), linked *via* a non-cleavable bifunctional linker (DARA-DM1). The near-infrared (NIR) fluorophore, IRDye800, was conjugated to DARA (DARA-IR) and DARA-DM1 (DARA-DM1-IR) to evaluate the mechanisms of action and biodistribution of the antibody constructs through two specific aims:

The first aim was focused on performing functional imaging of CD38 expression using bioconjugates of DARA in preclinical MM models. Conjugation of IRDye800 did not affect the stability or affinity of DARA *in vitro* and *in vivo*. Additionally, uptake of DARA-IR was significantly reduced in DARA-treated mice bearing intramedullary tumors, indicating a reduction in the expression of CD38. These observations are concordant with the known downregulation of CD38 in patients who do and do not respond to DARA therapy. Our results demonstrated the viability of using IRDye800 for sensitive, longitudinal assessment of the DARA antibody. DARA-IR can additionally be used as its own NIR contrast agent for monitoring CD38 expression *in vivo* in relation to DARA and other anti-CD38 therapies.

The second aim assessed the efficacy and mechanisms of DARA-DM1. Conjugation of DM1 improved antitumor efficacy of DARA *in vitro* and *in vivo*. Flow cytometry and fluorescence microscopy demonstrated similar binding and internalization of DARA-DM1-IR to DARA-IR in MM cells. Clearance of the DARA conjugates was primarily observed through the liver with no significant difference observed in tumoral uptake *in vivo*. Our observations validated that 1) DARA-DM1, compared to DARA, showed enhanced therapeutic efficacy and 2) the conjugation of IRDye800 does not affect the biologic activity or tumor targeting ability of the ADC.

In summary, these studies demonstrated the addition of a drug payload could enhance the therapeutic window of the native antibody. Fluorophore labelling allowed for evaluation of the different antibody constructs on a whole-body and cellular level in preclinical MM models. With the advent of other classes of anti-CD38 immunoconjugates for use in MM, we reasoned that such imaging techniques can be utilized to evaluate the tumor distribution and mechanism of

action of promising conjugates in preclinical MM models. Future studies would adapt this approach into different cell lines and humanized, immunocompetent tumor models.

Chapter 1: Introduction

1.1 Overview

Multiple myeloma (MM) is a debilitating hematologic malignancy of terminally differentiated plasma B-cells in the bone marrow (BM). It is the second most common hematologic malignancy and accounts for 15-20% of all hematologic malignancy-related mortalities. This chapter reviews the underlying biology of MM and cluster of differentiation 38 (CD38) and current treatment strategies and challenges with daratumumab (DARA). This is followed by a discussion on antibody drug conjugates (ADCs) as an emerging therapeutic strategy for relapsed and refractory MM patients as well as the use of fluorescence imaging for evaluation of novel therapies in preclinical MM. The section concludes with an overview of the two specific aims focused on enhancing DARA *via* conjugation of a cytotoxic payload and visualizing the uptake and distribution of the DARA ADC in preclinical MM.

1.2 Significance

1.2.1 *Multiple myeloma (MM) is a plasma cell dyscrasia with spatiotemporal heterogeneity*

Multiple Myeloma (MM) is an age-related cancer of differentiated plasma cells in the bone marrow (BM) and represents the second most common hematologic malignancy [1]. In the United States alone, there were over 30,000 estimated new cases and over 12,000 deaths in 2018. MM median 5-year survival has improved from 34.6% in 2004 to 49.6% in 2013. Myeloma pathogenesis involves precursor stages, monoclonal gammopathy of undetermined significance (MGUS) and smoldering multiple myeloma (SMM), before progressing to overt MM. Patients with MM suffer from debilitating fractures, anemia, renal failure, hypercalcemia and immune suppression. Relapse is almost certain and most that enter remission eventually die from relapsed

refractory disease, defined as those who become non-responsive or progressive on therapy. A recent analyses of patients with relapsed and refractory MM (RRMM), who were double refractory to frontline therapies of MM or had relapsed after > 3 prior lines of therapy showed a median overall survival (OS) of 8 months [2]. It is, therefore, imperative to identify efficacious treatments for RRMM patients.

Research on the molecular biology of myeloma-specific pathways and interactions with the BM environment has led to the development of treatment regimens with higher efficacy and reduced off-target toxicity, resulting in improved median survival from 2-3 years to over 7-8 years [3, 4]. A combination of drugs, including proteasome inhibitors, immunomodulatory agents, and small molecular chemotherapeutics is currently used to treat RRMM, typically as doublet or triplet regimens (Figure 1.1). However, therapy efficacy in the MM clinical population remains variable, especially at late stages in MM disease progression. MM drug resistance closely relies on tumor microenvironment. MM cells create a supportive niche with BM stromal cells, favoring MM cell survival through activation of several biological processes and modifying the surrounding tumor microenvironment. Accordingly, targeting both tumor and non-tumor cells is the main goal of new anti-MM therapeutic approaches.

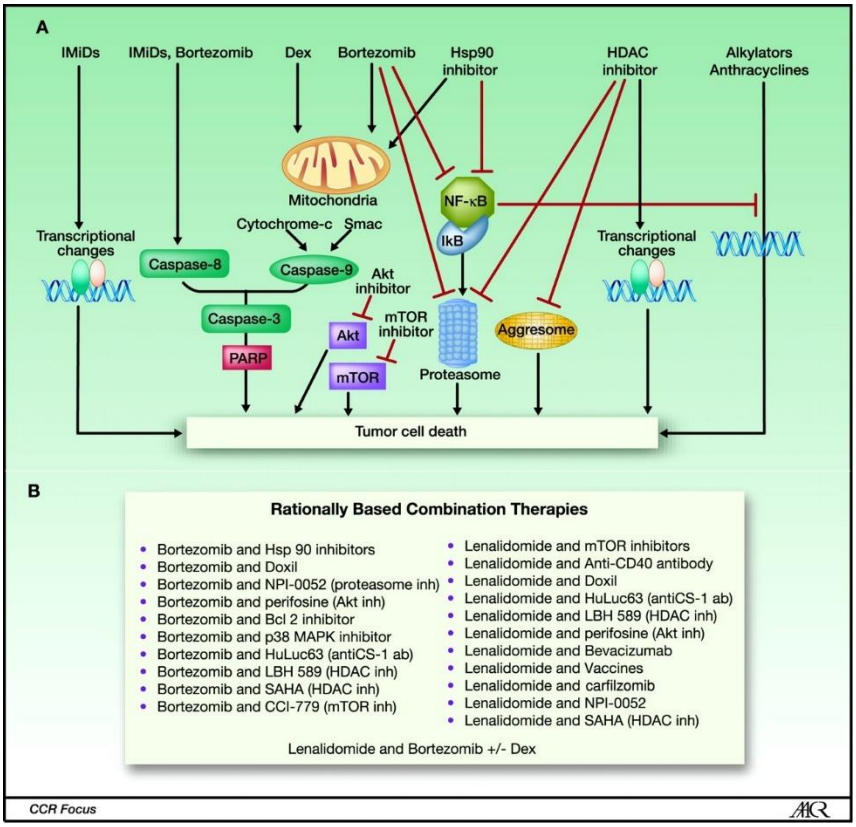

Figure 1.1: Schematic summarizing current treatment options for relapsed and refractory MM. Reprinted from [5].

1.2.2 *Cluster of differentiation (CD38) is a stable therapeutic target for MM double refractory patients.*

CD38 is a transmembrane protein, with both receptor and enzymatic functions, on the surface of myeloma cells and has been shown to co-regulate proliferation and differentiation of myeloid cells in conjunction with other receptors. Although normal lymphoid, myeloid, and some nonhematopoietic cells or tissues express CD38, MM tumor cells overexpress the receptor, thus providing a clinical rationale for the protein as a therapeutic target in MM. As a receptor, CD38 can mediate cell adhesion and migration through the tumor microenvironment, following ligation with agonistic mAbs or its natural ligand, CD31 (PECAM-1) [6]. As an enzyme, CD38

is known to hydrolyze nicotinamide adenine dinucleotide (NAD) to cyclic adenosine diphosphate ribose (cADPR), a potent metabolite that mobilizes calcium, and efficiently hydrolyzes its own cADPR to adenosine disphosphoribose (ADPR) [7]. Generation of cADPR and rapid calcium mobilization triggers the phosphorylation of different intracellular pathways such as activation of nuclear factor-κB complex, for overall cell proliferation and prolonged survival. Upon ligation with specific mAbs, CD38 on malignant cells prevents apoptosis and induces cytokines and protein-tyrosine phosphorylation [8–10]. The cytoplasmic domain of CD38 is short and lacks signaling motifs, docking sites and critical tyrosines for cytoplasmic associations with other functional receptors. The occurrence of CD38 in lipid rafts [11] further suggests that the regulation occurs through membrane movement of CD38 molecules in and out of specialized micro domains [12]. Figure 1.2 summarizes the mechanisms previously described in this section.

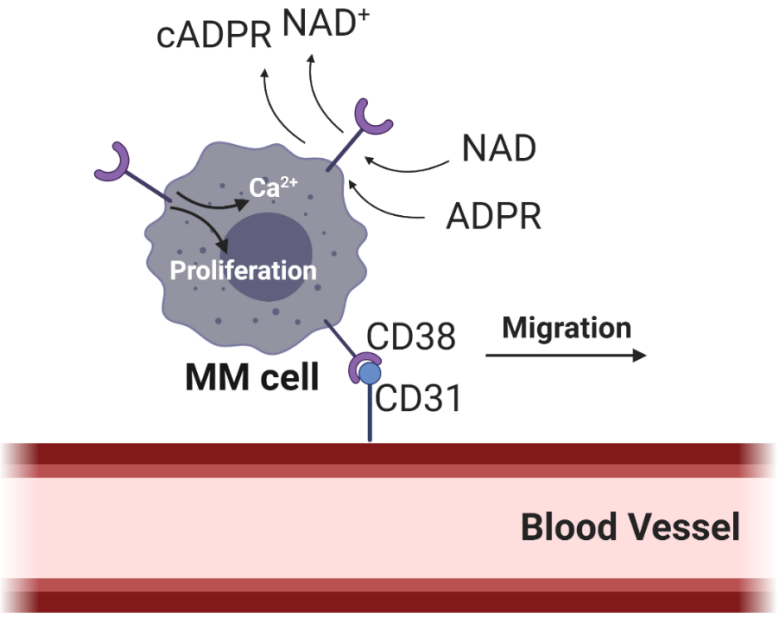

Figure 1.2: *Schematic summarizing the mechanisms of action of CD38 receptor. Created in BioRender.*

1.2.3 *Daratumumab (DARA) is a promising CD38-targeted immunotherapy for relapsed and refractory MM patients, but only shows partial response*

DARA was the first Food and Drug Administration (FDA)-approved, human immunoglobulin G1 kappa (IgG1k) monoclonal antibody that binds malignant cells expressing CD38 with high affinity. It mediates cell killing *via* Fc-dependent immune effector mechanisms including: complement-dependent cytotoxicity (CDC), antibody-dependent cell-mediated cytotoxicity (ADCC), antibody-dependent cellular phagocytosis (ADCP) and modulation of the enzymatic activity of CD38 [13–15]. In addition to the classic Fc-dependent mechanisms, DARA also has immunomodulatory effects by eliminating $CD38^+$ immune suppressor cells, such as regulatory T and B cells as well as myeloid-derived suppressor cells [16]. DARA-mediated elimination of these $CD38^+$ immune regulatory cells may reduce local immune suppression within the microenvironment and allowed for expansion of $CD4^+$ T-helper cells and $CD8^+$ cytotoxic T cells and contribute to anti-tumor response [16]. Figure 1.3 summarizes these mechanisms of action.

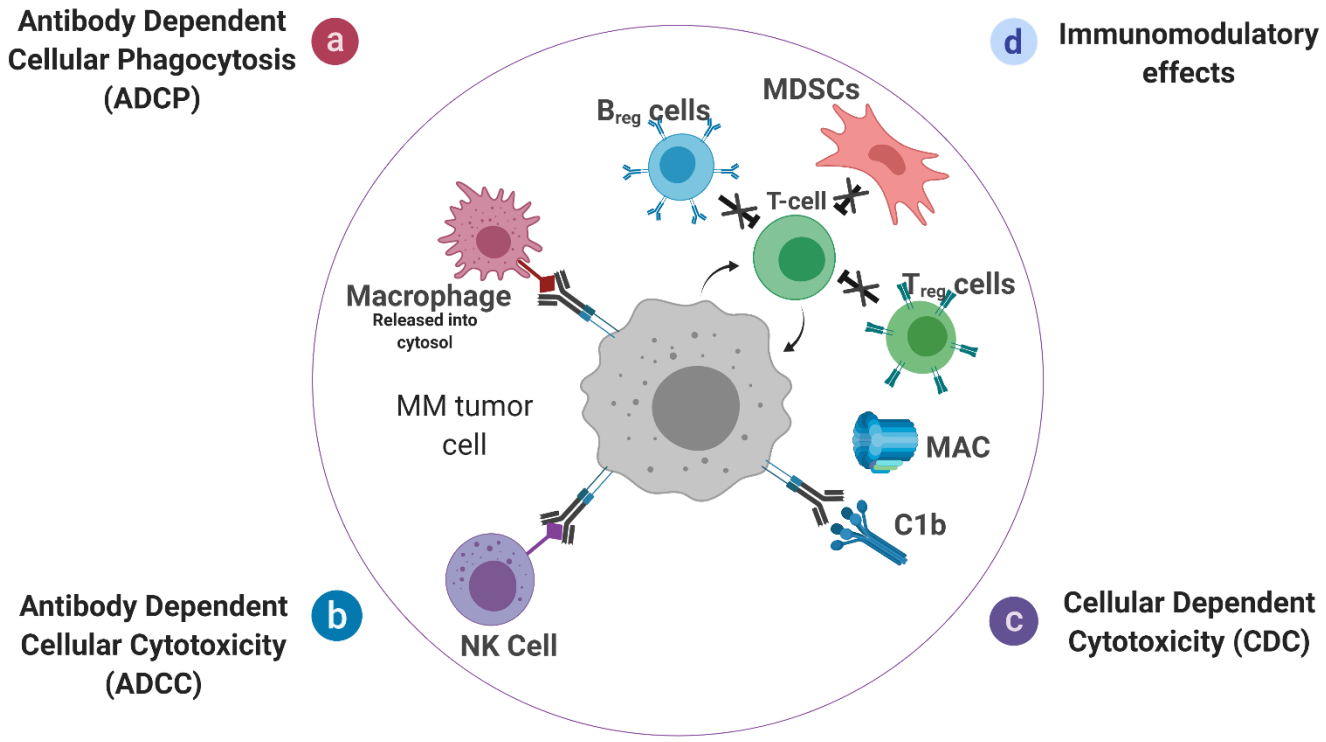

Figure 1.3: Schematic of the mechanisms of action of DARA. Created in *BioRender*.

CD38 expression on the surface of MM and non-tumor immune cells has been demonstrated to decrease following the first infusion of DARA due to trogocytosis, a phenomenon that involves the transfer of surface molecules from antigen-presenting cells to lymphocytes. In the case of DARA, it is suggested that the DARA-CD38 complex is transferred from MM to effector cells. While CDC and ADCC are reduced on MM cell surface, the continuous pressure by DARA to maintain MM cells in a $CD38^{low}$ state, either due to trogocytosis or internalization of the CD38 receptor, may contribute to effective anti-tumor immune response. As mentioned in Section 1.2.2, DARA interferes with the ectoenzymatic activity of CD38, reducing production of immunosuppressive adenosine [17]. Inhibition of CD38 has also shown to interfere with MM cell interactions in the BM microenvironment by reducing

expression of adhesion molecules on MM cells that allow for upregulation of proliferative pathways or transfer of mitochondria between BM stromal cells and MM cells [18]. It is still unclear how these immunomodulatory effects are directly correlated to DARA efficacy.

DARA has demonstrated durable responses as a monotherapy with no significant safety concerns. In the first-in-human phase 1-2 study GEN501, RRMM patients treated with DARA monotherapy at 16mg/kg showed an overall response rate (ORR) of 36% with median progression free survival (PFS) of ~6 months. Results from SIRIUS, a phase 2 study, demonstrated an ORR of 29% with median PFS of ~3 months [19]. Follow-up studies have demonstrated similar, deep responses of DARA monotherapy with median overall survival (OS) of 20.5 months and no significant safety concerns [20]. DARA has been shown to deplete natural killer (NK) cells, but to not affect its overall safety profile [21].

While DARA has shown promising results in such heavily pretreated patients, not all patients respond and the majority of patients who initially respond eventually progress. While the mechanisms are not entirely clear, a number of mechanisms have been proposed that are driving DARA resistance, summarized in Figure 1.4. One mechanism involves inhibition of the previously described mechanisms of action of DARA. Resistance to CDC and ADCC has been attributed to reduction of CD38 on MM tumor cells as previously mentioned and upregulation of complement-inhibitory proteins such as CD55 and CD59 [22]. ADCP and other immune-mediated mechanisms have been attributed to upregulation of CD28 and CD47 that act as "don't eat me" signals to protect MM cells while impairing environmental effector cells to mediate therapy [23].

Other environmental mechanisms driving DARA resistance have also been proposed. MM is characterized by clonal heterogeneity and high inter- and intra-lesion genetic diversity. It

has been shown that DARA may preferentially kill high CD38-expressing MM cells, allowing for the expansion of MM cells with low CD38 ($CD38^{low}$) expression with reduced CDC and ADCC activity [24]. In addition to trogocytosis, Horenstein et al. demonstrated that DARA binding to CD38 induces a redistribution of CD38 antigens into polar aggregates, released as microvesicles into the BM microenvironment that produce adenosine [25]. The increase in adenosine in the BM niche allows for the release of proinflammatory cytokines, inhibiting anti-MM immune responses [26].

In addition to the upregulation of such immunomodulatory pathways, a decrease in effector cell populations that play a key role in DARA-mediated tumor killing has also been observed in DARA resistant patients. Low numbers of effector memory T cells [16] and M1 macrophages [27] in non-responders has been documented. RNA sequencing of MM BM stromal cells depleted of $CD138^{+}$ MM cells demonstrated that immune response-regulating genes such as TLR8, CD47, CXCL10 and CXCL4 were most downregulated in gene pathways of DARA progressing patients (those who had discontinued DARA therapy for at least 4 weeks prior to analysis) compared to untreated patients [28]. Cell killing assays using peripheral blood mononuclear cells (PBMCs) obtained from DARA progressing patients did not demonstrate an ability to kill $CD38^{+}$ MM cells in the presence of DARA [28]. Cell separation of PBMCs based on CD38 expression showed no killing effect in MM cells treated with DARA in the presence of $CD38^{low}$ PBMCs [28]. This suggests that immune-mediated pathways may be contributing to DARA binding on $CD38^{+}$ immune effector cells, not just on MM cells, leading to further DARA resistance.

The efficacy of DARA has shown to significantly improve in combination with other frontline therapies of MM and improve many of DARA's immune-mediated mechanisms

previously mentioned. DARA has been approved in combination with bortezomib or lenalidomide and dexamethasone in RRMM patients as well as in combination with melphalan and prednisone in patients with newly diagnosed MM. Both combination therapies were well tolerated and resulted in rapid, deep, durable responses with ORR of 82.9% for DARA plus lenalidomide/dexamethasone [29] and 81% for DARA plus bortezomib/dexamethasone [30]. An estimated 42-month OS rate of 75 percent for patients treated with DARA plus bortezomib, melphalan and prednisone was observed with more prolonged progression free survival compared to patients treated without DARA [30]. Preclinical studies have demonstrated that this synergy may be due to the increased DARA-mediated lysis from increased activation of autologous immune cells. Nijhof et. al. demonstrated that lenalidomide improved MM tumor killing in combination with DARA in both lenalidomide-sensitive and -resistant MM tumor cells, possibly due to the stimulation of NK cells from lenalidomide and not *via* direct effects on the tumor cells [31, 32]. In addition to the re-introduction of frontline therapies, all-*trans* retinoic acid (ATRA) combination therapies are also being explored, as ATRA has shown to increase CD38 levels to pretreatment values and decrease CD55 and CD59 expression [22]. This has resulted in significant enhancement of CDC and ADCC activity.

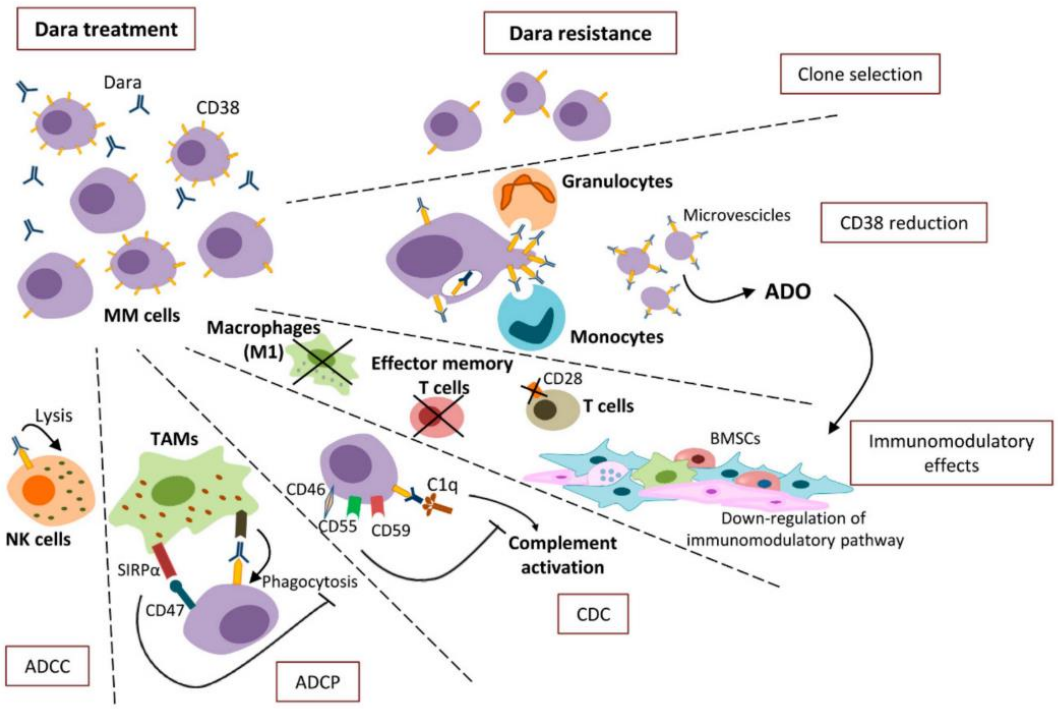

Figure 1.4: Summary of the mechanisms of resistance of DARA. Reprinted from [23].

1.2.4 *Summary*

MM is a highly clonal disease that is significantly influenced by its tumor microenvironment. CD38 is a promising target on MM cells and is involved in many physiological processes of lymphocytes where it is upregulated. DARA is an anti-CD38 monoclonal antibody that has shown significant outcomes, both as a monotherapy and in combination therapies, in RRMM patients. Despite significant and ongoing advances, 60% of patients do not achieve deep and durable responses and will eventually relapse during therapy due to upregulation of inhibitory proteins and clonal heterogeneity in available effector immune cells [33]. Given the immunosuppressive nature associated with RRMM patients, there is a need for novel anti-CD38 therapies with unique mechanisms of action that can induce apoptosis without a sole reliance on effector immune cells. While we recognize the advent of other anti-

CD38 radiotherapies, immunotoxins and immunotherapies that bind to different CD38 epitopes, the focus of this thesis will primarily be on the use of antibody-drug conjugates (ADCs).

1.3 Antibody Drug Conjugates (ADCs) enhance the efficacy of immunotherapies

1.3.1 *Introduction*

One possibility for enhancing the potency of antibodies and increasing its therapeutic index is to introduce additional drugs to complement the multiple mechanisms of action of the native immunotherapy. ADCs combine the highly targeted tumor antigen recognition of antibodies with the cell killing properties of chemotherapy for effective internalization and processing of the drug. Typically, the ADC will: 1) recognize and attach to the target receptor 2) internalize the ADC-antigen complex into the cell *via* receptor-mediated endocytosis 3) breakdown the ADC by lysosomal proteins for release of the free cytotoxic warhead (Figure 1.5).

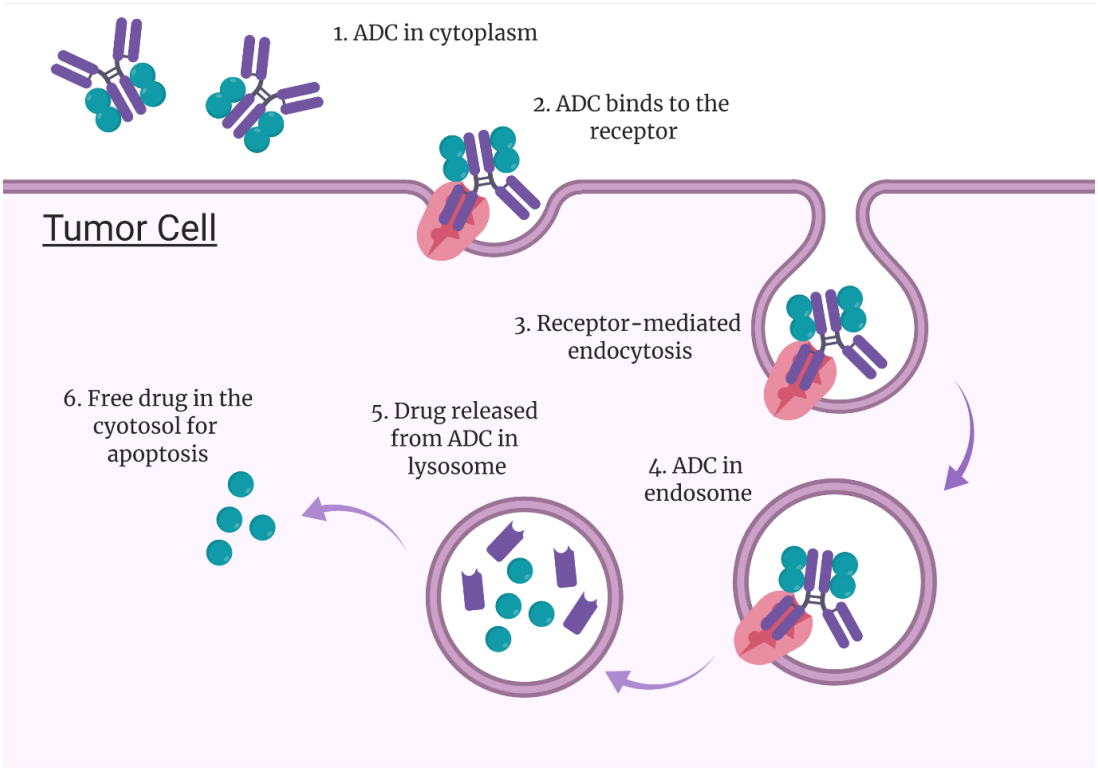

Figure 1.5: Schematic of ADC mechanism of action. Created in *BioRender*.

The ADC can possibly retain all the mechanisms of action of the native antibody while introducing an additional mechanism to overcome drug insensitivity associated with RRMM patients. The following sub-sections will focus on a discussion of linkers and drug payloads typically used in ADCs.

1.3.1.1 Linkers

Linkers play a key role in the efficacy and safety of an ADC. They must be stable enough in circulation to avoid any off-target toxicities from early release of the payload while efficiently releasing said payload in the cytosol following trafficking in specific subcellular compartments. The choice of linker is also target dependent, based on how well the antibody-target antigen complex can internalize and degrade. Furthermore, the choice of a linker is also influenced by the drug payload, as each molecule has different chemical constraints. There are primarily two types of linkers used in ADCs: non-cleavable and cleavable. Due to the chemical and metabolic nature of tumor cells, cleavable linkers each have a unique mechanism of cleavage with their own advantages and disadvantages, summarized in Table 1.1. Linkers are typically attached at either a lysine or cysteine group on the antibody. While lysine-based conjugation *via N*-hydroxysuccinimide (NHS) esters allows for greater drug loading with a stable amide bond, there is also a heterogeneous distribution of drug loading with some antibodies loaded with more drug than others, leading to greater variability in therapeutic efficacy [34, 35]. Cysteine-based conjugation, conversely, relies on maleimide chemistry, which allows for more site-specific conjugation and uniform drug loading of the antibody. Maleimide-based ADCs, however, can have reduced *in vivo* stability due to presence of blood thiols, particularly albumin, which can cause non-specific release of payload through the retro-Michael reaction [34, 35].

Cleavable linkers typically rely on either the intracellular conditions of the cytosol or the

extracellular conditions of the target cell to facilitate drug release. The two major mechanisms of cleavage involve acid-labile and enzymatic degradation. Mylotarg (anti-CD33) and Besponsa (anti-CD22) are two examples of clinically-approved ADCs for blood cancers that use acid-labile hydrazine linkers, which are designed to remain stable at neutral pH of blood circulation, but undergo hydrolysis and release of the cytotoxic drug in the acidic environment of cellular components [36]. Adcetris (anti-CD30), Polivy (anti-CD79b) and Zynlonta (anti-CD19) rely on dipeptide linkers such as valine-citrulline and valine-alanine that are cleaved by intracellular, tumor-associated lysosomal cathepsin B for rapid hydrolysis [36–38]. While it is difficult to compare these two cleavable linkers, both are often associated with broader efficiency of killing (due to the bystander killing effect on neighboring cells, particularly antigen-negative tumor cells), but suffer from limited plasma stability, particularly with acid-labile linkers that have demonstrated early release of drugs in the bloodstream [39]. The challenge remains to modulate release of drug payloads without inducing off-target toxicities in antigen-positive non-tumor cells. Current research efforts are primarily focused on introducing more steric hindrance using substituents near the linkage to improve the overall serum stability. New cleavable linkers, such as disulfide linkers, are being developed with unique cleavage mechanisms and are continued to be tested in ADCs. Such linkers can be modified with sulfonate groups to increase hydrophilicity and reduce the aggregation and non-specific toxicities characteristic of ADCs.

Converse to cleavable linkers, non-cleavable linkers resist proteolytic degradation, requiring complete lysosomal degradation of the biologic. Blenrep (anti-BCMA) is the most recent example of a MM-specific ADC that uses one class of non-cleavable linkers, a maleimidocaproyl linker, to deliver its cytotoxic payload. Despite the instability of the maleimide attachment site, hydrolysis of the thiosuccinimide ring has shown to eliminate early

cleavage due to retro-Michael reaction [34, 35]. The other major class of non-cleavable linkers are disulfide linkers, primarily succinimidyl-4-(*N* maleimidomethyl)-cyclohexane-1-carboxylate (SMCC), that consist of a thioether bond that creates steric hindrance in the linker [34, 35]. While ADCs with non-cleavable linkers typically have reduced potency compared to those with cleavable linkers due to the lack of bystander effect, they have greater *in vivo* stability and more efficient intracellular drug release. Non-cleavable ADCs, however, are highly dependent on the biology of the target receptor and the antibody-receptor complex to internalize for effective delivery of drug to tumors. In contrast, ADCs with cleavable linkers may still be active against targets that poorly internalize.

Linker	**Release mechanism**
Hydrazone	Cleaved in acidic tumor microenvironment
Peptide	Enzymatically hydrolyzed by lysosomal proteases such as *cathepsin B*
Disulfide	Non-cleavable or cleavable through disulfide exchange with intracellular thiol, such as glutathione
Thioether	Non-reducible and designed for intracellular proteolytic degradation

Table 1.1: Summary of release mechanisms of types of cleavable and non-cleavable linkers for ADCs.

1.3.1.2 Maytansinoid drug payloads

In addition to the linker, the appropriate drug payload needs to be selected for an ADC. As there are often only a limited number of antigens on the tumor cell surface and the average drug-to-antibody ratio (DAR) of the most current clinical-stage ADCs is limited to 3.5-4, the payload not only needs to be highly cytotoxic in the sub-nanomolar range, but also be soluble

and stable under physiological conditions. Typical drug payloads will target organelles inside the cell, such as DNA or microtubules, since most ADCs heavily rely on cell internalization for release the payload in the cell. Maytansinoids account for the cytotoxic payloads in a majority of ADCs undergoing clinical trial, specifically mertansine (DM1) and ravtansine (DM4) [40]. They are potent microtubule inhibitors that bind to tubulin and destabilize microtubule minus-end attachment to centrosomes and spindle poles, inducing mitotic arrest in the target cell and preventing cell division [41, 42]. These two drugs are previously failed anticancer agents due to their systemic toxicity and poor therapeutic window [43]. However, they have been selected as candidate payloads due to the high potency (ED_{50} (effective dose) of 10^{-4} and 10^{-5} µg/mL), excellent water solubility following conjugation, stability under physiological conditions and suitability for the attachment of stable linkers. All of these parameters play key roles in the metabolism and cytotoxicity of the maytansinoid payload [44]. Most maytansinoid linkers rely on disulfide linkers for attachment to the antibody: DM1 typically relies on non-cleavable SMCC linkers while DM4 relies on cleavable linkers such as N-succinimidyl -4-(2-pyridyldithio) butanoate (SDPB) and N-succinimidyl -4-(2-pyridyldithio) pentanoate (SPP). When DM4 is cleaved at the disulfide bridge, either the drug or the uncharged, S-methylated drug is released, allowing for passive diffusion into antigen-negative tumor cells (bystander effect) [45]. Conversely, the positive charge of the metabolite of DM1-conjugated antibodies (lysine-SMCC-DM1) has a net positive charge, which allows for greater cell retention and subsequent reduced bystander effect [46, 47]. While cleavable conjugates with the bystander effect have shown superior efficacy over non-cleavable conjugates, these conjugates may also lead to non-specific toxicities in healthy cells. Therefore, a balance must be identified between *in vivo* stability and efficient intracellular drug release to maximize the therapeutic window.

1.3.2 *Conclusions*

The goal of the ADC is to allow for a greater percentage of drug molecules to reach tumors, thereby lowering the minimum effective dose and increasing the maximum tolerated dose. ADCs are highly modular in nature, leading to numerous combinations of antibodies, linkers and drug payloads. Each component can influence the stability, cytotoxicity and pharmacokinetics of the overall ADC. Given the differences in biology between different cancers, each factor needs to be considered to construct the ideal ADC candidate.

1.4 Near-infrared fluorescence imaging provides high-throughput preclinical functional imaging

1.4.1 *Introduction*

The visualization and quantification of tissue biodistribution and uptake of a therapeutic agent can provide significant insights into its on- and off-target potential toxicities and pharmacokinetics. Molecular imaging can serve as a powerful tool to evaluate these parameters and provide significant insights into designing next-generation therapeutic agents with superior safety and efficacy. Positron Emission Tomography (PET) and Single-Photon Emission Computed Tomography (SPECT) are routinely used for *in vivo* imaging of novel therapeutics. While both modalities are highly sensitive and can quantify tissue uptake, the use of decaying radioisotopes and ability to trace just one molecular species (in the case of PET) does not allow for simultaneous imaging of multiple targets.

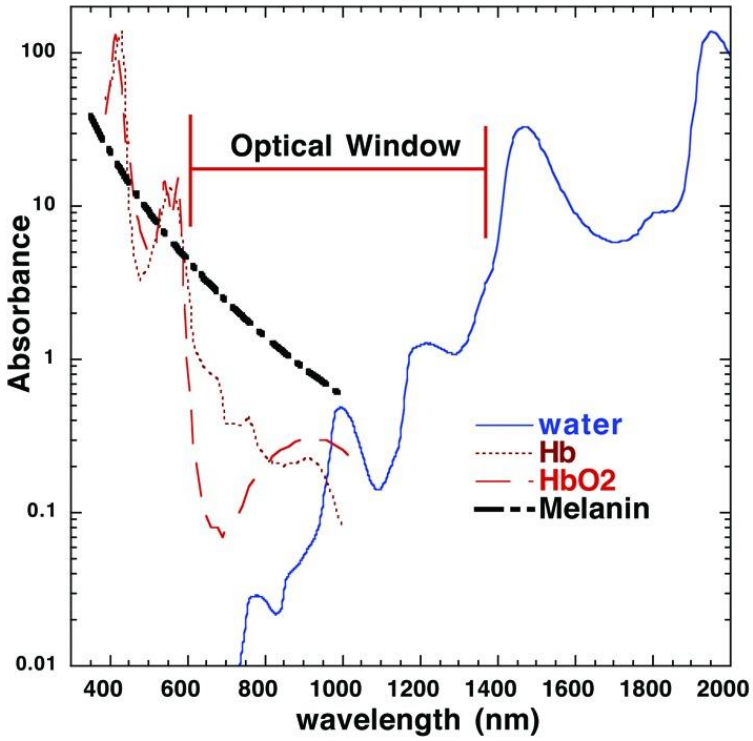

Figure 1.6: Absorption spectra of common tissue components. Hb, deoxygenated hemoglobin; HbO2, oxygenated hemoglobin. Reprinted from [48].

One preclinical alternative is to use near-infrared (NIR) fluorescence imaging, which is both low cost and high-throughput. Using a NIR imaging strategy allows for deep signal penetration through endogenous chromophores in the visible wavelength spectrum. The absorption coefficients of hemoglobin and melanin decrease significantly after 600nm and water does not increase significantly until after 1200nm, creating an "optical window" in the NIR wavelengths of 700-900nm that maximizes penetration of light into the skin [48] (Figure 1.6). Optical imaging also allows for multiplexing biomarkers, due to the availability of multiple wavelengths that can be utilized, for non-invasive, longitudinal imaging of the spatial distribution and interactions between targets without the need to sacrifice mice.

NIR fluorescence imaging of antibody-based therapies typically involves labelling with

an NIR fluorophore such as AlexaFluor or Cyanine dye *via* an NHS ester or maleimide reactive group, allowing the dye to be attached to a number of antibodies *via* an amide or cysteine group, respectively. Fluorescently-labelled monoclonal antibodies have routinely been used in preclinical research for evaluation of receptor expression on a cellular and whole-body level. Other NIR-conjugated antibody constructs such as affibodies [49–52], $F(ab')_2$ fragments [53, 54], bispecific antibodies [55] and ADCs [56–59] have also been developed not only for imaging the receptors the agent targets, but also to evaluate the agent's uptake and biodistribution in preclinical models of solid cancer. This dissertation will explore the use of IRDye800CW, a NIR dye (Ex./Em. 774nm/810nm) that exhibits deeper tissue penetration and a higher photostability than Cyanine 5.5 (Cy5.5) (Ex./Em. 684nm/710nm) due to the longer excitation wavelength. IRDye800 has routinely been labelled to monoclonal antibodies for preclinical [60–63] and clinical use [64–66] and has shown no pathological evidence of toxicity *in vivo* [67].

1.4.2 *NIR fluorescent imaging in preclinical models of MM*

Despite the advances in novel antibody-based therapies in MM, there have been limited published studies involving fluorescently labelling these antibodies for imaging in MM or other hematologic cancers. This is partly due to the limited spatial resolution of fluorescent imaging methods in such models. Although the optical window affords increased light penetration, tissue turbidity, presence of large macromolecules, and other chromophores cause scattering. The diffuse nature of MM tumors (primarily residing in the bone) in myeloma mice also prevents sufficient uptake of fluorescently-conjugated agents for longitudinal, *in vivo* imaging, despite the greater depth penetration and reduced autofluorescence. Despite these drawbacks, recent advances in targeting moieties and improved technologies for real-time fluorescence imaging in small animal models have allowed for visualization of such biologics in relation to molecular

processes in the BM microenvironment.

Current efforts in optical imaging of preclinical MM are focused on several bone- and tumor-specific NIR tracers. A review of these tracers has been published in *Journal of Bone Oncology* [68]. Commercial bone-specific probes such as OsteoSense and BoneTag use fluorescently-labelled bisphosphonates that target hydroxyapatite (HA)-active regions on the mineralized bone surface and have routinely been used to study bone turnover in metastatic prostate and breast cancer models. Fluorescently-tagged Cathepsin-B (ProSense) and -K (Cat K FAST) as well as matrix metalloproteinases (MMPSense) target pro-osteolytic factors that are stimulated by cancer cells to promote matrix degradation and bone fracture [69, 70]. In preclinical MM models, AngioSense is a NIR blood pool vascular agent that has been used, in conjunction with other fluorescently-labelled MM cells, to visualize BM vasculature using *in vivo* flow cytometry and confocal microscopy [71, 72]. While MM-specific fluorescent probes are limited, fluorescently-conjugated LLP2A has shown promise as an imaging agent in MM and lymphoma models. LLP2A is a high-affinity peptidomimetic ligand for the activated form of the receptor of Very Late Antigen-4 (VLA-4), which plays a vital role in mediating adhesion of MM tumor cells to the BM stroma for improved survival and trafficking [73]. *In vivo* optical imaging of LLP2A in mouse xenografts has shown high sensitivity and specificity to VLA-4 expressing tumor cells [74, 75]. These studies show promise for bone-specific *in vivo* imaging for preclinical MM models. Additionally, exogenous fluorophores can be combined with transfection models that express luciferase or fluorescent proteins for spatial registration of markers. Optical imaging of our DARA-based conjugates in intramedullary, immunocompromised MM mice is explored in this dissertation.

1.4.3 *Conclusions*

Optical imaging is an emerging tool for evaluating the mechanisms of action and tissue distribution of novel biologics on a whole-body and cellular level in preclinical models of cancer. Various imaging approaches in the NIR-I window have been developed to multiplex such biologics in relation to the bone and other molecular processes in the microenvironment. Such imaging can complement current clinical imaging modalities, particularly PET- or SPECT-CT, to enable real-time, longitudinal assessment of biologics on a functional, structural and molecular level.

1.5 Specific aims and Dissertation outline

1.5.1 *Specific aims*

We hypothesize that conjugation of: 1) IRDye800 would allow for visualization of the biologic activity and tumor targeting ability of the native DARA 2) DM1 should enhance tumor-killing efficacy of the native DARA and its mechanism of action and biodistribution can be monitored *via* fluorescence imaging. With the advent of other classes of immunoconjugates for use in MM [76], we reasoned that such labelling techniques can be used to evaluate the tumor distribution and mechanism of action of other conjugates in preclinical MM models.

Aim 1: Develop a fluorescently-labelled DARA for targeted imaging in preclinical MM.

Aim 2: Enhance cytotoxicity of DARA with DM1 and use fluorescence imaging to visualize uptake and biodistribution of fluorescent ADC.

1.5.2 *Dissertation outline*

Chapter 1 provides an overview of CD38 biology in MM, DARA therapy and associated mechanisms of resistance, ADCs and current optical imaging strategies in preclinical MM.

In vitro and *in vivo* evaluation of IRDye800-conjugated DARA (DARA-IR) is covered in Chapter 2. DARA-IR was additionally used to assess CD38 expression during DARA therapy. Uptake was validated using *ex vivo* flow cytometry and planar fluorescent biodistribution.

In Chapter 3, the microtubule inhibitor, mertansine (DM1), was conjugated *via* non-cleavable bifunctional linker to DARA (DARA-DM1). Therapeutic efficacy of DARA-DM1 was compared to the native DARA. IRDye800 was used to label both DARA conjugates for subsequent *in vitro* and *in vivo* evaluation of their stability, binding and internalization.

Finally, the general conclusions, limitations, and future work are discussed in Chapter 4.

Chapter 2: Preclinical Development of Near-Infrared Labelled CD38-Targeted DARA for Optical Imaging of CD38 in MM

2.1 Overview

In this study, we demonstrate the use of NIR fluorescence imaging for spatiotemporal monitoring of the DARA antibody and CD38 expression in preclinical MM using DARA-IR. Despite the well-established clinical efficacy of DARA in RRMM patients, not all heavily pretreated patients respond to single-agent DARA therapy, and the majority of patients who initially respond eventually progress. As new anti-CD38 therapies with novel mechanisms of action (MoA) are being developed to overcome DARA resistance, understanding the predictive value of CD38 expression and its relation to DARA and therapeutic efficacy will be key for identifying the ideal candidate CD38 antibodies for new treatment regiments. Therefore, a strategy to evaluate CD38 expression spatiotemporally in preclinical models could inform physicians on implementing similar strategies for other antibody therapies in the pipeline. Current methods to evaluate CD38 expression in the preclinical setting include *ex vivo* flow cytometry and immunohistochemistry, which can be cumbersome and do not give whole-body

information. *In vivo* imaging technologies such as PET rely on decay of radioisotopes, limiting the number of molecular interactions observed at any given time point.

Here, we demonstrate the use of NIR fluorescence imaging for spatiotemporal monitoring of CD38 expression in preclinical MM using DARA conjugated to the NIR fluorophore IRDye800CW (DARA-IR). DARA-IR maintained stability and had high affinity for CD38 (K_D = 3.5 $\pm$ 0.05 nM). DARA-IR demonstrated a 5- and 18-fold increase in contrast in tumor-bearing regions of mice with extra- and intramedullary MM. Finally, mice treated with therapeutic doses of DARA and imaged with DARA-IR showed an 11-fold decrease in fluorescence intensities *in vivo* compared to untreated controls. Our studies establish DARA-IR as a promising contrast agent for preclinical evaluation of CD38 expression and for further investigating myeloma engraftment and kinetics in relation to anti-CD38 therapies. The material covered in this chapter is published in the journal *Molecular Imaging and Biology* [77].

2.2 Introduction

CD38 is a surface receptor expressed on myeloid, lymphoid and non-hematopoietic cells [78] and is overexpressed on malignant cells in patients with MM, leukemia and lymphoma [18, 79]. CD38-targeted monoclonal antibodies (mAbs) have either been approved for clinical use (i.e. DARA) or are undergoing evaluation (i.e. isatuximab and MOR-202) in RRMM patients [80]. Each of these immunotherapies exhibit their own unique mechanisms of apoptosis and bind to different epitopes on the CD38 receptor. While mAbs such as DARA rely on recruitment of effector cells, removal of $CD38^+$ immune-suppressor cells and apoptotic activity via secondary cross-linking of mAbs [13], isatuximab uniquely inhibits the enzymatic activity of CD38 and directly induces apoptosis without cross-linking [81].

As new CD38 mAbs with novel MoA are being developed for MM and other diseases,

understanding the predictive value of CD38 expression and its relation to therapeutic efficacy will be key for identifying the ideal candidate CD38 antibodies for new therapy regiments. While DARA has been extensively studied [22, 82], the MoA of CD38 in relation to other anti-CD38 therapies are still limited. Therefore, a strategy to evaluate CD38 expression spatiotemporally in preclinical models could inform physicians on implementing similar strategies for other mAbs in the pipeline. Traditional means of detecting receptor expression, such as *ex vivo* multi-color flow cytometry and histopathology, can provide valuable information on CD38 with respect to individual immune cells and other cellular markers, but can be time-consuming and labor-intensive. Such methods can also make it difficult to temporally assess CD38 expression during therapy in relation to processes such as angiogenesis and cell migration in the presence of an intact bone marrow microenvironment. There is an unmet need for a reliable whole-body imaging technique to assess whole CD38 expression quickly and accurately in these diffuse tumors for preclinical drug evaluation.

Recently, antibody-based imaging has emerged as a powerful tool for noninvasive, longitudinal imaging of functional markers due to the low toxicity and high specificity of such probes [83]. Our group has previously demonstrated the use of DARA as a companion diagnostic for PET imaging in preclinical mouse models of MM [84]. While PET is a highly sensitive imaging modality in MM diagnosis, it allows for monitoring of one molecular species and does not allow for the simultaneous tracking of interactions between molecular targets [85]. NIR fluorescence overcomes this limitation and is routinely used for imaging in preclinical animal models due to its reduced autofluorescence in the visible wavelength range (400-600nm) and its ability for multiplexing of fluorescence signals at different emission wavelengths between contrast agents and fluorescently transfected cells [86]. This provides valuable functional

information on biological processes involved in MM and associated therapies in preclinical animal models.

In this study, we evaluated DARA conjugated to the NIR dye IRDye800CW (Ex./Em. 774nm/810nm) (Li Cor) (DARA-IR) for fluorescent imaging in MM animal models. DARA was chosen as the candidate anti-CD38 for these studies due to its approval in the clinic in addition to its high specificity to CD38 and low toxicity [19]. We hypothesized that the enhanced specific expression of CD38 glycoprotein on malignant plasma cells will favor increased DARA-IR uptake. The proof-of-principle *in vitro* and *in vivo* data in $CD38^+$ human myeloma cells and MM mouse models demonstrated the potential of DARA-IR for both *in vivo* and *ex vivo* evaluation of CD38 expression in response to DARA therapy. These studies will contribute toward providing tools for monitoring CD38 expression in relation to novel anti-CD38 therapies evaluated in preclinical models for MM and other diseases in general.

2.3 Materials and Methods

2.3.1 *Fluorescent labelling of monoclonal antibody*

Daratumumab (DARA) (Darzalex, Janssen, Beerse, Belgium) was generously donated by the Center of Advanced Medicine pharmacy at Washington University School of Medicine. Control IgG (Sigma Aldrich) and DARA were conjugated to the NIR dye, IRDye800CW NHS ester (Li Cor, Lincoln, NE, USA) according to the manufacturer's instructions. Briefly, antibodies were reacted at an antibody concentration of 5mg/mL in 0.1M potassium phosphate buffer (pH 8.5) for 2 hours. Dye to antibody molar ratio of 3 to 1 was used. Unconjugated dye was removed by desalting zeba spin columns (Sigma Aldrich). The degree of labelling (DOL) was determined using the DU-640B spectrophotometer (Beckman Coulter) to measure fluorophore absorbance at 774nm and antibody absorbance at 280nm, corrected for the

fluorophore (Figure 2.1). The DOL is defined as the average dye to protein concentration ratio. After purification, conjugates were run on sodium dodecyl sulfate-polyacrylamide gel electrophoresis (SDS-PAGE) (Bio-Rad, Hercules, CA, USA) in the presence of human serum (Sigma Aldrich) at 37°C at incubation intervals of 1, 3, 7 and 8 days. Gels were scanned using the Odyssey CLx (Li Cor) measured at the 800nm channel and images were analyzed in Image Studio Version 5.2 software (Li Cor).

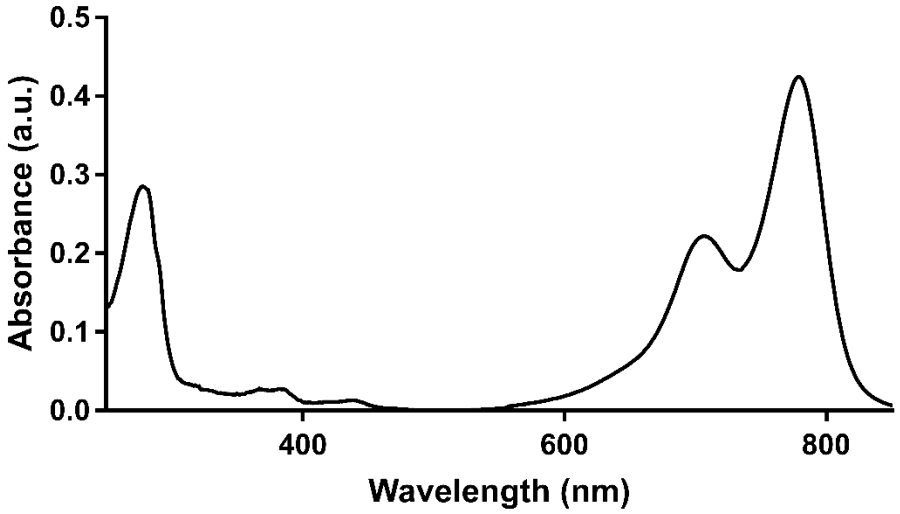

Excess Molar Ratio	280nm Absorbance	Dye Max Absorbance	Protein Conc. (μM)	Dye Conc. (μM)	DOL
3	0.2835	0.4233	1.76	1.45	1.2

Figure 2.1: Antibody-dye absorbance spectra of DARA-IR. After reaction and purification, the absorbance spectrum for DARA-IR was used to determine the DoL as described in the methods section. DoL was determined by dividing bulk fluorophore concentration by antibody concentration.

2.3.2 *Cell Culture*

The human myeloma MM.1S cells were obtained from ATCC and modified to express click beetle red luciferase and green fluorescent protein (MM.1S-GFP-luc) by the DiPersio

laboratory (Professor John F. DiPersio, Washington University School of Medicine, St Louis, MO, USA). Cells were cultured in Roswell Park Memorial Institute 1640 medium (Thermo Fisher Scientific) supplemented with 10% heat inactivated fetal bovine serum and 1% Gentamicin (Sigma Aldrich).

2.3.3 *In vitro saturation binding assay*

DARA-IR at various concentrations (0.675 – 33.76nM) was incubated with $2.5x10^5$ MM.1S-GFP-luc cells in triplicate for 3 hours at 37°C. Our group has previously confirmed high expression of the CD38 antigen on MM.1S-GFP-luc cells [84]. Cells were then washed twice in 1X phosphate-buffered saline (PBS). Flow cytometry was performed on the LSR Fortessa (BD) to calculate mean fluorescence intensities (MFI) of bound DARA-IR. 7-aminoactinomycin D (Thermo Fisher Scientific) $(7AAD)^-/GFP^+$ population was considered as viable tumor cells and used for statistical analysis. Blue laser (Ex. 488nm) was used to detect 7AAD (Em. 695/40nm) and GFP (Em. 530/30nm) while red laser (Ex. 640nm) was used to detect IRDye800 (Em. 780/60nm). Non-specific binding was determined by incubating MM.1S-GFP-luc cells with excess unlabeled (100-fold) DARA. Flow cytometry data was analyzed with FlowJo Version 10.6.2 software (BD). Competitive binding curves were fitted to obtain the K_D of DARA-IR using GraphPad Prism Version 7 based on the non-linear fitting curve that compensates for the non-specific binding (one-site total and non-specific binding) (GraphPad Software Inc.).

2.3.4 *Animal models*

All animal studies were performed in accordance with the Institutional Animal and Use Committee of Washington University School of Medicine. Mice were anesthetized for all treatments and imaging with 2% v/v isoflurane/100% O_2. Female 1-3 month old fox chase severely combined immunodeficient (SCID) mice (Charles Rivers Laboratories) were injected

with $3x10^6$ MM.1S-GFP-luc cells in 100µL 1X PBS subcutaneously (MM.1S SQ) or intravenously (MM.1S IV) *via* lateral tail vein. Tumor burden was monitored every 3-4 days *via* bioluminescence imaging (BLI) (Figure 2.2A) and mice were weighed (Figure 2.2B) prior to administration of DARA-IR in both mouse models. For imaging studies in MM.1S SQ and IV models, mice were randomized into respective cohorts when a mean photon flux of $1x10^9$ photons/second was achieved. Healthy, female SCID mice of the same age were used for biodistribution studies as non-tumor mouse controls.

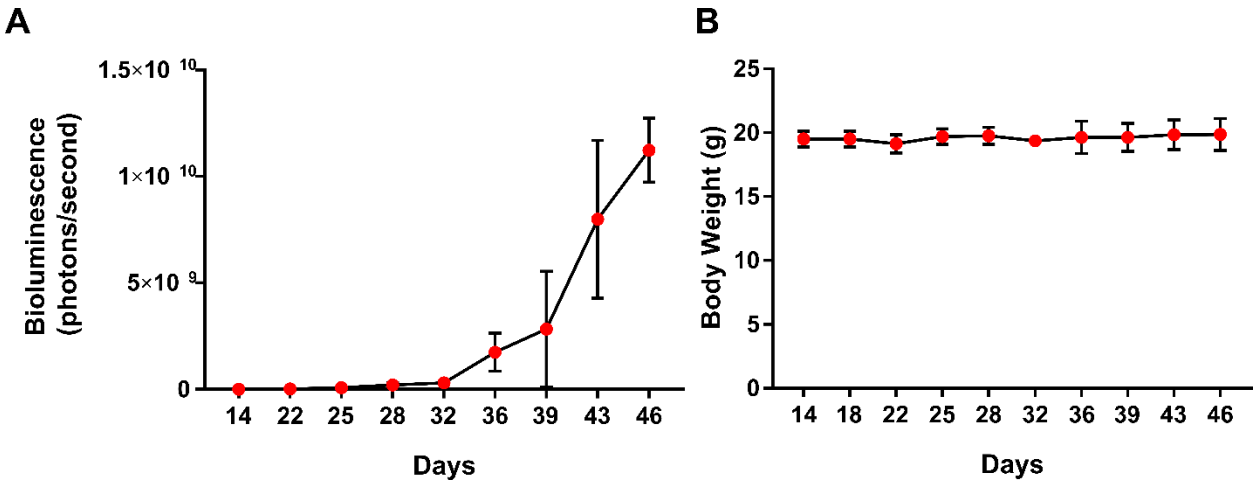

Figure 2.2: Mean A) bioluminescence and B) body weights of MM.1S IV mice (n = 5) following intravenous injection of MM.1S-GFP-luc cells.

2.3.5 *In vivo and ex vivo fluorescent imaging*

DARA-IR and IgG-IR, respectively, was administered intravenously (IV) in MM.1S SQ and MM.1S IV mice (n = 5/group) at 4mg/kg of body weight in 1X PBS. Daily optical imaging in the GFP (Ex./Em. 480nm/535nm) and IRDye800 channels (Ex./Em. 785nm/820nm) was performed up to 7 days following injection using the Optix MX3 time-domain diffuse optical imaging system (Advanced Research Technologies, Montreal, Canada). Prior to imaging, hair was removed by gentle clipping and depilatory cream to improve light transmission. Following

imaging, mice were sacrificed at appropriate time points and tissue was excised. GFP (Ex./Em. 480nm/535nm) and IRDye800 (Ex./Em. 780nm/820nm) fluorescent images of excised tissue were acquired on the MX FX Pro In-Vivo System (Bruker) and Pearl Small Animal Imager (Li Cor), respectively. Tumor to background ratios (TBRs) were calculated from IRDye800 fluorescent images of MM.1S SQ mice by dividing the MFIs from regions of interest (ROIs) drawn in ImageJ (NIH) software around GFP^+ tumor regions by the MFIs from non-tumor (background) regions on the contralateral side of the mouse. For MM.1S IV images, MFIs were also measured from ROIs drawn around GFP^+ tumor regions using ImageJ software and compared to MFIs prior to injection of DARA-IR. *Ex vivo* GFP and IRDye800 fluorescent images were analyzed in ImageJ and Pearl Cam Version 2.0 (Li Cor) software, respectively, by measuring MFIs from ROIs drawn around bone and muscle tissue. Tissue to muscle ratio was calculated by dividing MFIs of bone tissue by MFIs of muscle tissue of each respective mouse.

2.3.6 *Plasma clearance*

Plasma clearance was measured in MM.1S IV mice (n = 5/group). Prior to administration of DARA-IR, whole blood was obtained through cheek bleeding of mice. At 2 and 7 days post-administration of DARA-IR, whole blood was collected from mice by terminal cardiac puncture procedure. Plasma was obtained by mixing 15µL of the whole blood with 15µL of PBS-Ethylenediaminetetraacetic acid disodium salt dihydrate (EDTA) (10mM) (Corning Life Sciences), centrifuging at 3000g for 1 minute and freezing the resulting plasma at -80°C. The concentration of fluorescent antibody was determined by scanning 15µL of plasma on the Odyssey CLx at the 800nm channel. Normalized clearance was determined by dividing the signal intensity of plasma at the different time points by the intensity from plasma obtained pre-administration of DARA-IR.

2.3.7 *Biodistribution*

MM.1S SQ, MM.1S IV and non-tumor SCID mice were anesthetized, bled and dissected 2 and 7 days after injection of DARA-IR IV at 4mg/kg of body weight. Whole tumor and non-tumor tissues were dissected for biodistribution studies to quantify IRDye800 fluorescent tracer in units of percentage of injected dose per gram of tissue (%ID/g) as previously described [87]. Briefly, organs were suspended in 1mL 1X PBS and then homogenized by mechanical disruption using the Mini Beadbeater 24 (Biospec Products) for 1 minute. After homogenization, 150µL of organs were pipetted into clear bottom 96-well black plates (Corning Life Sciences). The NIR fluorescence intensity of the samples was measured at the 800nm channel with the Odyssey CLx. The signal intensity was compared to a calibration curve and normalized to organ weight and homogenate volume to compute %ID/g. Calibration standards were made with increasing concentrations of DARA-IR in 1X PBS.

2.3.8 *Ex vivo flow cytometry*

Viable cells were obtained from tibial and femoral bone marrow flush from MM.1S IV mice, washed in fluorescence activated cell sorting buffer (made with 1X PBS, 0.5M EDTA and 0.5% Bovine Serum Albumin (Sigma Aldrich)), stained and immediately analyzed with LSR Fortessa. For GFP^+ tumor graft viability, $7AAD^-/GFP^+$ population was considered as viable tumor cells. Laser channels and FlowJo Version 10.6.2 software were used as previously described.

2.3.9 *DARA therapy study*

Weekly BLI was performed on MM.1S IV mice until they reached a mean photon flux of $3x10^6$ photons/second. Mice were then randomized into untreated and treated cohorts (n=7/group). Treated mice were provided DARA intraperitoneally (IP) at a therapeutic dose of

16mg/kg of body weight in 1X PBS. Treatment was administered weekly for 6 weeks in accordance with DARA treatment guidelines [88]. Additional BLI was performed twice per week during therapy. Relative bioluminescence was calculated for each time point by dividing photon flux by baseline photon flux prior to therapy. After 6 weeks, mice from treated and untreated cohorts were injected IV with DARA-IR at 4mg/kg of body weight in 1X PBS. Mice were imaged on Optix MX3 time-domain diffuse optical imaging system and immediately sacrificed at 7 days post administration for *ex vivo* biodistribution and flow cytometry studies as previously described. Analysis of *in vivo* fluorescent images was performed in ImageJ by measuring MFIs from whole-body ROIs drawn around mice. Normalized fluorescence intensities were calculated by dividing MFIs post-contrast by MFIs prior to DARA-IR administration. *Ex vivo* images and flow cytometry data were analyzed as previously described with an additional stain performed with PE mouse anti-human CD38 (BD) for flow cytometry.

2.3.10 *Statistical Analysis*

All data is presented as mean $\pm$ standard deviation and statistical analysis was performed using GraphPad Prism Version 7 software. Statistical significance between cohorts was calculated using student t-test and two-way analysis of variance (ANOVA) followed by Sidak's multiple comparisons test, unless specified otherwise. P values of less than 0.05 were considered statistically significant.

2.4 Results

2.4.1 *In vivo serum stability and saturation binding assay*

DARA-IR maintained > 95% of its initial fluorescent signal by day 8, indicating minimal dye deconjugation and formation of free dye during incubation (Figure 2.3A). DARA-IR also demonstrated saturable binding to $CD38^+$ MM.1S human myeloma cells. The dissociation

constant (K_D) of DARA-IR was calculated to be 3.5 ± 0.05nM and the receptor density (B_{max}) of DARA-IR was calculated to be 5.6 ± 0.13nM (Figure 2.3B), validating the high binding affinity of DARA-IR to MM.1S myeloma cells.

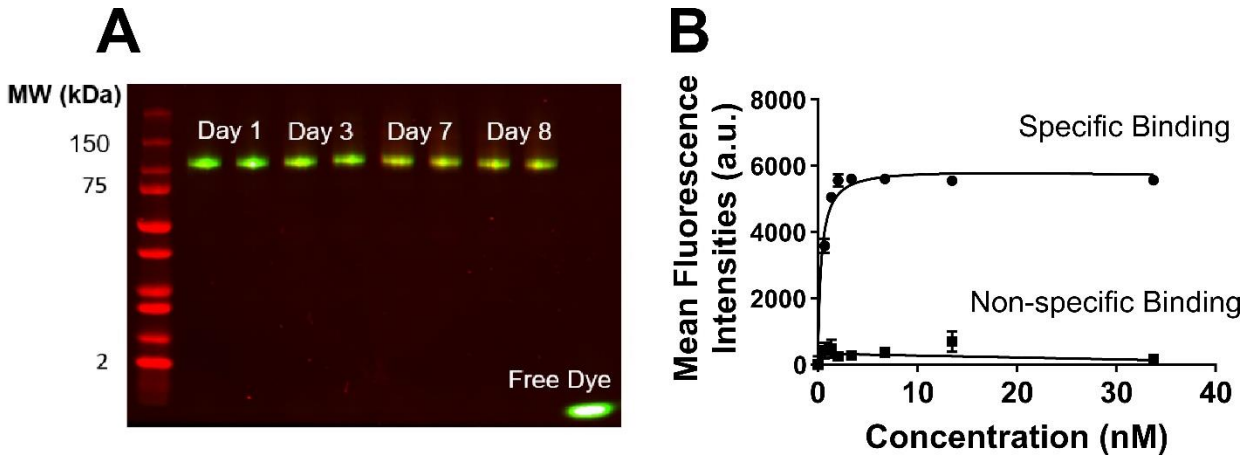

Figure 2.3: *In vitro* evaluation of stability and binding of DARA-IR. A) SDS-PAGE of DARA-IR incubated in human serum between 1-8 days. Free dye represents unmodified IRDye800 NHS ester. B) Flow cytometric saturation binding assay showing specific and non-specific binding of DARA-IR to $CD38^+$ MM.1S cells. n =3/group.

2.4.2 *High specificity of DARA-IR conjugate to $CD38^+$ extramedullary MM tumors*

To quantify contrast and the optimal imaging time point of DARA-IR, MM.1S SQ mice were injected IV with the fluorescent conjugate. Significant uptake of DARA-IR was observed in GFP^+ tumor-bearing regions by day 7 of fluorescent imaging (Figure 2.4A) with a peak TBR of 5.84 ± 0.85 (Figure 2.4B). This time point was later used for imaging intramedullary tumors in MM.1S IV mice. Tissue biodistribution studies were in agreement with the *in vivo* fluorescent imaging data. Tumor uptake was calculated to be 9.3 ± 2.95 %ID/g at day 7. Clearance of the conjugate was observed primarily through the liver with peak uptake of 6.04 ± 1.58 %ID/g at day 2 (Figure 2.4C) and 2.56 ± 1.15 %ID/g at day 7. Liver uptake in non-tumor mice was more than

3-fold greater at both time points (Day 2: 20.62 ± 1.99 %ID/g; Day 7: 8.24 ± 6.5 %ID/g). No statistically significant differences were observed in other non-tumor tissue between MM.1S SQ and non-tumor mice.

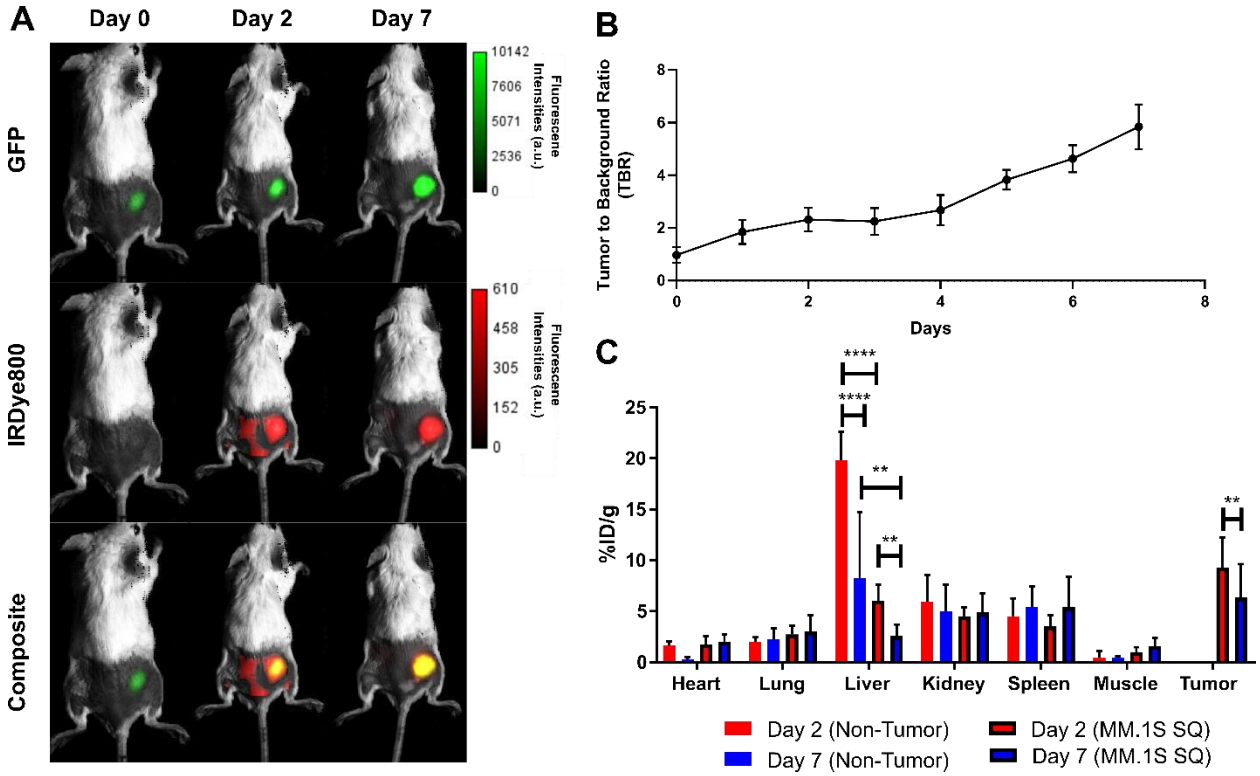

Figure 2.4: High contrast observed with DARA-IR at longer time points in MM.1S SQ mice. A) Representative GFP and IRDye800 *in vivo* images of MM.1S SQ mice 2 and 7 days post administration of DARA-IR. B) Calculated TBRs in MM.1S SQ mice across individual time points of DARA-IR. C) Normalized biodistribution (%ID/g) at 2 and 7 days post administration of DARA-IR in non-tumor and MM.1S SQ mice. n = 5/group. Two-way ANOVA followed by Sidak's multiple comparisons test was performed on biodistribution data. **p < 0.01; ****p < 0.0001. a.u.: arbitrary units.

2.4.3 *High specificity of DARA-IR conjugate to CD38^{+} intramedullary MM tumors*

In vivo fluorescent imaging of DARA-IR was also performed in MM.1S IV mice. DARA-IR showed high specificity to GFP^{+} tumors in marrow-rich regions of the tibia (Figure 2.5A), skull (Figure 2.5B) and spine (Figure 2.5C) with an 18-fold increase in MFIs by day 7 (Figure 2.6A).

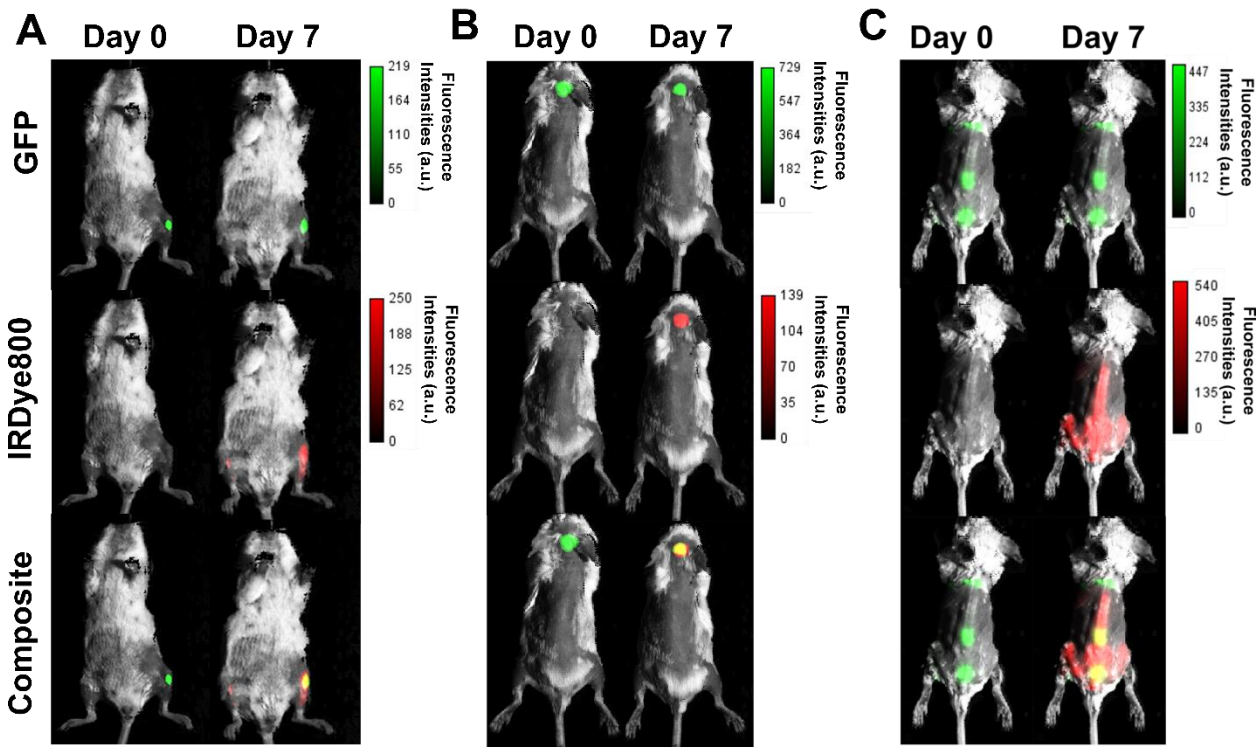

Figure 2.5: DARA-IR allows for non-invasive imaging of cancerous bone marrow regions in MM.1S IV mice. Representative images of GFP and IRDye800 fluorescence *in vivo* of A) femur B) skull C) spine in separate MM.1S IV mice 7 days post administration of DARA-IR. a.u.: arbitrary units.

Ex vivo fluorescent imaging of bones and non-tumor tissue from MM.1S IV mice administered with non-specific IgG conjugated to IRDye800CW (IgG-IR) showed a 5-fold difference in MFIs in tumor-bearing regions compared to mice administered with DARA-IR

(Figure 2.6B). Tissue biodistribution studies demonstrated clearance of DARA-IR primarily in liver and spleen with peak uptake of 17.64 ± 3.69 and 16.75 ± 7.53 %ID/g, respectively (Figure 2.6C,D). Statistically significant differences in uptake between non-tumor and MM.1S IV mice were observed in spleen at day 2 (Non-tumor: 4.86 ± 1.73 %ID/g; MM.1S IV: 16.75 ± 7.53 %ID/g), liver at day 7 (Non-tumor: 8.24 ± 6.5 %ID/g; MM.1S IV: 2.73 ± 1.23 %ID/g) and kidney at day 2 (Non-tumor: 6.17 ± 2.82 %ID/g; MM.1S IV: 1.49 ± 0.9 %ID/g) and day 7 (Non-tumor: 5.0 ± 2.57 %ID/g; MM.1S IV: 0.49 ± 0.18 %ID/g). A 4-fold decrease in fluorescence intensity of plasma was observed by day 7 (Figure 2.6E). Viable, GFP$^+$ tumor cells flushed from tibial and femoral bone marrow of mice administered with DARA-IR and IgG-IR were analyzed by flow cytometry and showed significantly increased expression of DARA-IR (MFI: 12651 ± 2134) relative to IgG-IR (MFI: 1842 ± 35.13) (Figure 2.6F).

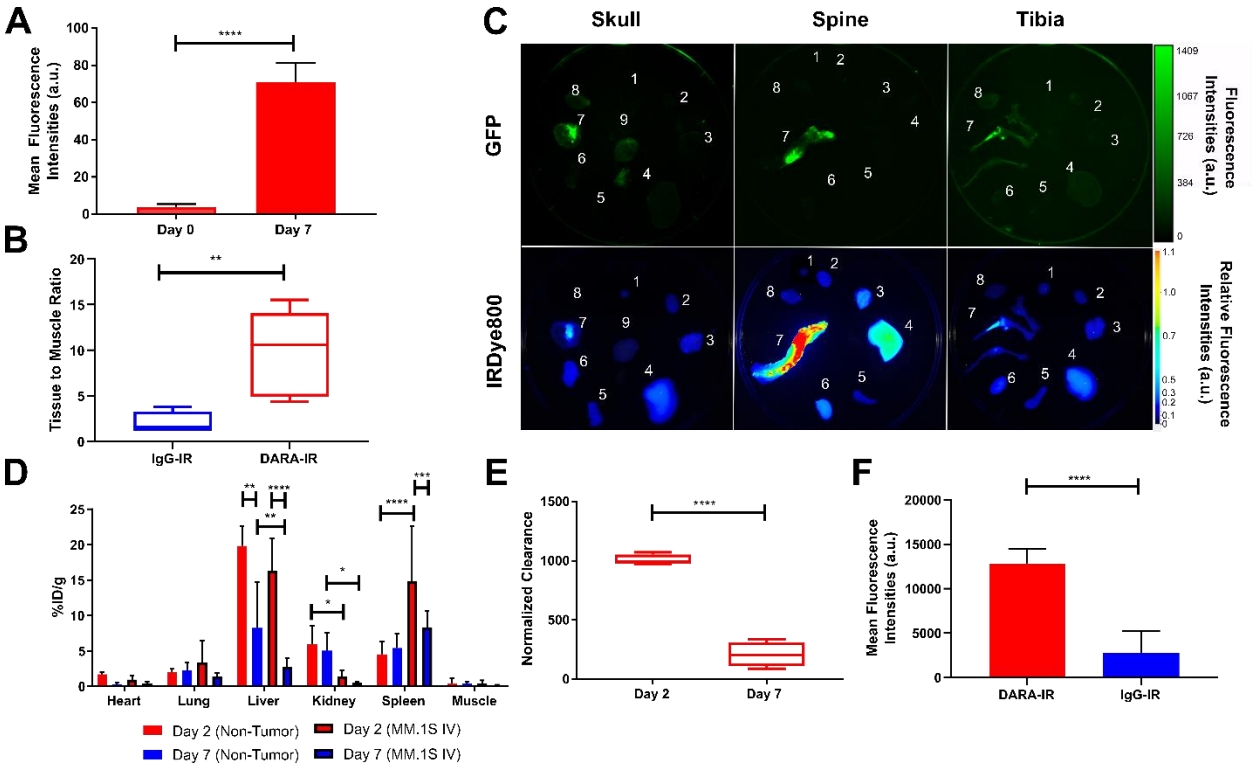

Figure 2.6: Biodistribution and flow cytometric analysis of DARA-IR in MM.1S IV mice.

A) MFIs of DARA-IR in GFP$^+$ tumor regions from *in vivo* animal images 7 days post

administration. B) Tissue to muscle ratios of DARA-IR and IgG-IR from *ex vivo* images of GFP^+ bones. C) Representative GFP and IRDye800 fluorescent images of 1) blood 2) heart 3) lung 4) liver 5) spleen 6) kidney 7) bones (skull, spine, pelvis and leg bones) 8) muscle 9) brain. D) Normalized biodistribution (%ID/g) at 2 and 7 days post administration of DARA-IR in non-tumor and MM.1S IV mice. E) Normalized plasma clearance of DARA-IR 2 and 7 days post administration. F) Flow cytometric analysis of IRDye800 MFIs from excised bone marrow of DARA-IR and IgG-IR control. n = 5/group. Two-way ANOVA followed by Sidak's multiple comparisons test was performed on biodistribution data. Student t-test was performed on all other datasets. *$p < 0.05$; **$p < 0.01$; ***$p < 0.001$; ****$p < 0.0001$. a.u.: arbitrary units.

2.4.4 *DARA-IR detects changes in CD38 expression during DARA therapy*

A proof-of-principle therapy study was conducted to validate the use of DARA-IR in noninvasively monitoring CD38 expression following CD38-targeted therapies. Mice treated with DARA showed an 11-fold decrease in normalized IRDye800 fluorescence intensities *in vivo* compared to untreated mice (Figure 2.7A,B). Efficacy of DARA therapy in MM.1S IV mice was validated with BLI (Figure 2.7C). *Ex vivo* imaging of bones from both mouse cohorts confirmed our *in vivo* imaging results.

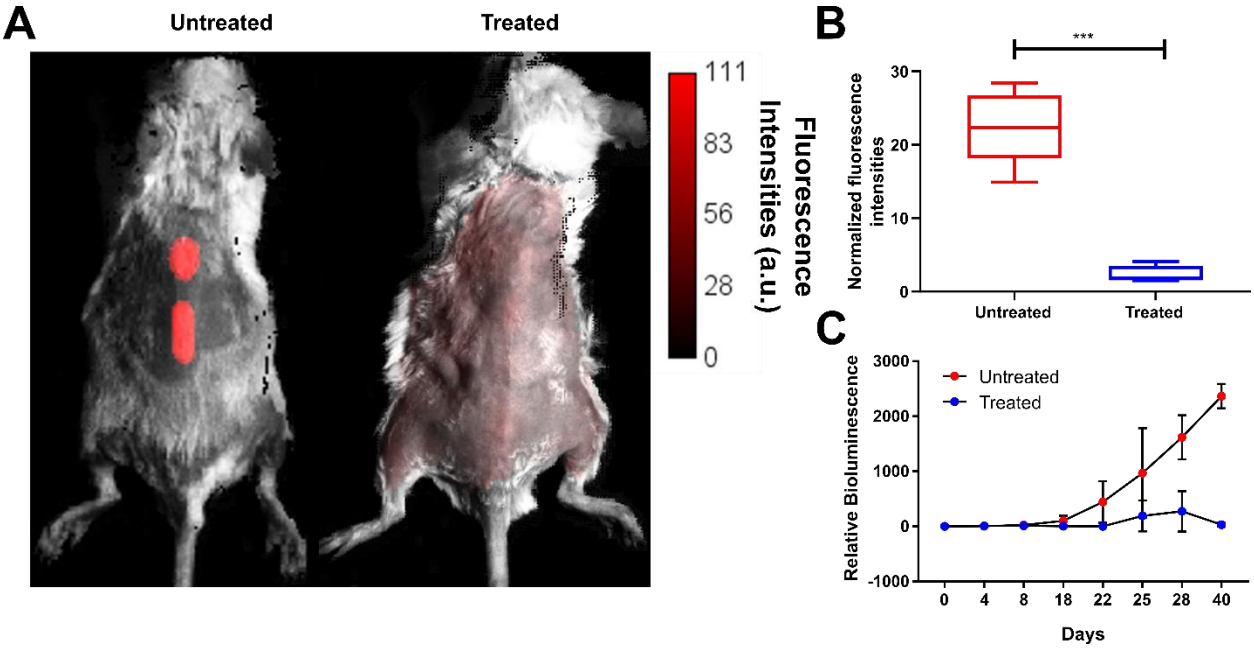

Figure 2.7: Changes in DARA-IR fluorescence intensities observed *in vivo* with respect to therapy. A) Representative *in vivo* images of IRDye800 fluorescence in mice treated and untreated with DARA therapy. B) MFIs of bone regions normalized to pre-contrast MFIs of DARA-IR from *in vivo* animal images of untreated and treated mice. C) Longitudinal BLI of DARA therapy prior to mouse sacrifice. n = 7/group. Student t-test was performed on normalized fluorescence intensities. ***p < 0.001. a.u.: arbitrary units.

Tissue to muscle ratios of bones from IRDye800 and GFP channels were significantly higher in untreated mice (IRDye800: 8.51 $\pm$ 5.1; GFP: 1.36 $\pm$ 0.5) compared to treated mice (IRDye800: 2.07 $\pm$ 1.16; GFP: 0.58 $\pm$ 0.18) (Figure 2.8A,B). Biodistribution of DARA-IR was statistically not significant across other non-tumor tissue (Figure 2.8C). Flow cytometry on excised bone marrow validated *in vivo* and *ex vivo* images and showed a statistically significant decrease in MFIs of DARA-IR between treated (MFI: 12841 $\pm$ 1627) versus untreated (MFI: 2790 $\pm$ 2419) mice (Figure 2.8D). No significant difference in MFIs of the commercial PE-

conjugated CD38 antibody was observed between treated (MFI: 101.84 ± 75.81) and untreated (MFI:133.66 ± 58.5) mice.

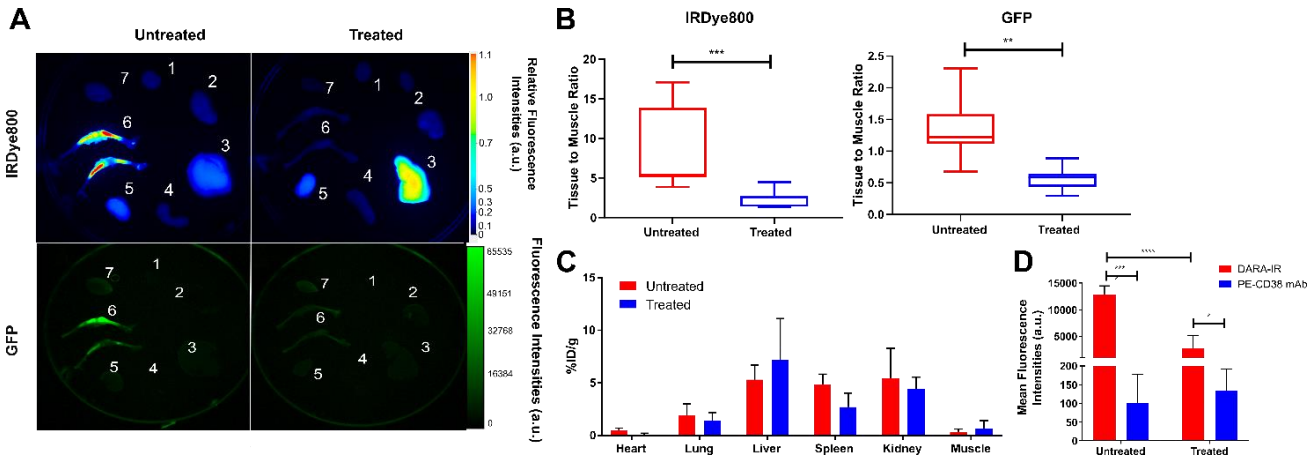

Figure 2.8: Biodistribution and flow cytometric analysis of changes in DARA-IR with respect to therapy. A) Representative IRDye800 and GFP fluorescent images of excised 1) heart 2) lung 3) liver 4) spleen 5) kidney 6) leg bones 7) muscle from MM.1S IV mice untreated and treated with DARA at a therapeutic dose. B) MFIs of bone regions normalized to MFIs of muscle tissue for IRDye800 and GFP between untreated and treated cohorts. C) Normalized biodistribution (%ID/g) of DARA-IR in untreated and treated mouse cohorts following sacrifice. D) Flow cytometric analysis of DARA-IR and commercial PE-conjugated human anti-CD38 (PE-CD38 mAb) MFIs in GFP^+ viable tumor cells from excised tibial and femoral murine bone marrow. n = 7/group. Two-way ANOVA followed by Sidak's multiple comparisons test was performed on biodistribution data. Student t-test was performed on all other datasets. *p<0.05, **p < 0.01, ***p<0.001, ****p<0.0001. a.u.: arbitrary units.

2.5 Discussion

To date, there are few NIR fluorescent contrast agents for use in hematologic malignancies such as MM *in vivo*. Most *in vivo* imaging strategies are primarily focused on transfection of fluorescent encoding vectors such as enhanced green fluorescent protein (eGFP)

for tracking of whole tumor cell populations [89]. While retroviral transfection of fluorescent proteins is routinely used to monitor cell and protein expression, these reporter constructs require time-consuming methods for modulation of the native protein and typically use fluorescent proteins in the visible range (400–645nm) that may not have sufficient brightness and contrast for *in vivo* imaging [82]. Molecular imaging in the NIR I range (650-950nm) is an alternative strategy for preclinical evaluation of expression levels in the presence of therapy [68].

Antibody-based probes directed toward tumor-associated antigens have become promising contrast agents. Optically-labelled $F(ab')_2$ fragments from panitumumab ($PaniF(ab')_2$) and bevacizumab ($BevF(ab')_2$) have been developed for noninvasively measuring epidermal growth factor receptor and vascular endothelial growth factor, respectively, in the presence of different anti-angiogenic therapies in animal models [90, 91]. We reasoned that DARA-IR could be similarly used as a non-invasive, relatively inexpensive means of rapidly validating CD38 expression in animal models of MM and other hematologic diseases. The ease of functional fluorescence imaging, compared to PET, can potentially increase experimental throughput compared to other methods such as *ex vivo* flow cytometry on excised bone marrow tissue and can allow for spatiotemporal monitoring of CD38 expression in the presence of the bone marrow microenvironment.

We were able to demonstrate that the conjugation of the dye to the native antibody did not affect the specificity of DARA in both MM.1S SQ and IV mouse models. The K_D of DARA-IR to MM.1S was calculated to be 3.5 ± 0.05nM, which is consistent with the affinity of native DARA (4.36nM) [13, 88]. Furthermore, our plasma stability studies demonstrate that there was little fallout of free dye following conjugation, suggesting that fluorescence intensities are due to binding of DARA-IR and not due to non-specific uptake of unbound free dye.

Our *in vivo* imaging results in both MM.1S SQ and IV mice showed that DARA-IR had high specificity to GFP^+ tumor lesions. MM is a plasma cell disorder that causes significant skeletal morbidity and disruption of osteoclast and osteoblast activity within the bone marrow niche [4]. As anticipated, DARA-IR uptake was observed in bone marrow regions in MM.1S IV mice including skull, pelvis, spine and long bones. Our *in vivo* results demonstrate the potential for noninvasive, whole-body imaging of CD38 in diffuse tumors within the bone marrow of MM mice.

Ex vivo biodistribution studies showed significant clearance through liver, spleen and kidney by day 7 in MM.1S SQ and non-tumor mice. Due to their large size (~150 kDa), IgG mAbs such as DARA are primarily catabolized *via* the liver [92] with some catabolism in the spleen and kidney [93]. In addition, DARA has a half-life of 18 days [88], which matches the long half-life of DARA-IR. Both factors may have contributed to high uptake of the fluorescent probe in spleen and kidney in MM.1S SQ and non-tumor mice.

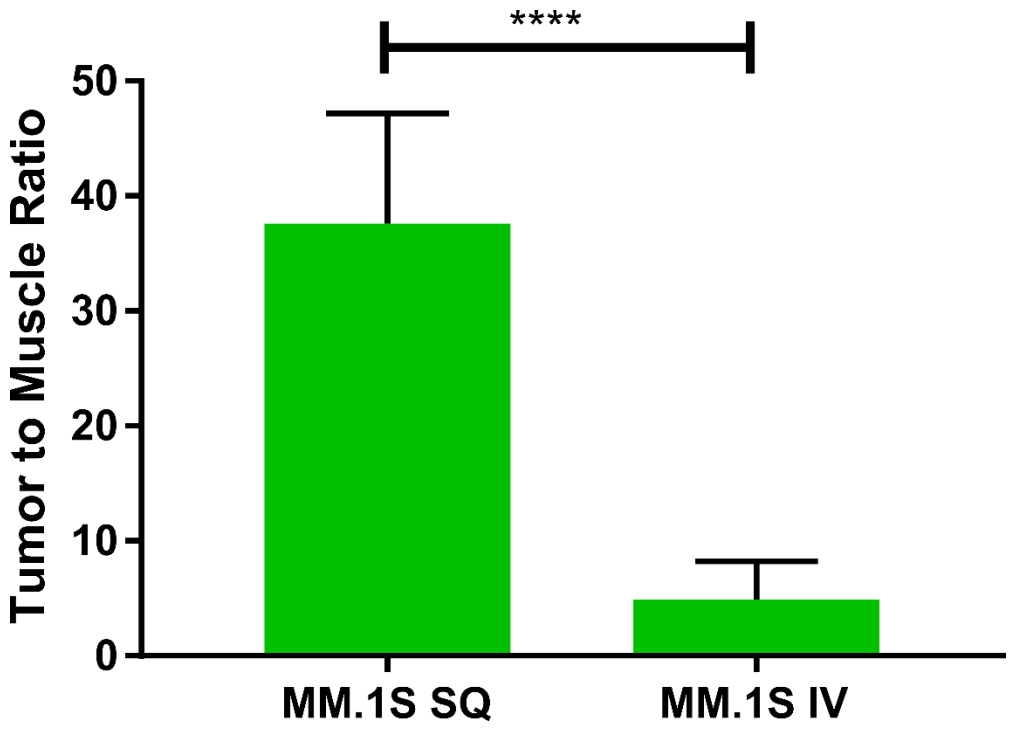

Figure 2.9: MFIs of GFP+ tumor regions normalized to MFIs of muscle tissue (tumor to muscle ratio) for MM.1S SQ and MM.1S IV mice. n = 5/group. Student t-test was performed. ****p < 0.0001.

While SQ injection of myeloma cells into SCID mice typically results in tumor growth at the sight of injection with rarely any systemic disease, IV injection of human myeloma cells results in diffuse tumor growth in variable regions of bone marrow in mice [94]. Normalized GFP fluorescence intensities from *ex vivo* organ images demonstrated greater tumor burden in the MM.1S SQ mice than in the bone tissue of MM.1S IV mice (Figure 2.9). Additionally, circulating tumor cells, abnormal paraprotein secretion in the serum and subsequent renal impairment, and tumor engraftment in the liver have been demonstrated following IV injection of human myeloma cells in SCID mice [94]. These factors are reflective of clinical MM and are likely contributing to greater uptake of DARA-IR in the liver and spleen with poor kidney clearance in the MM.1S IV mice.

We have demonstrated that DARA-IR can be used for monitoring CD38 expression in the presence of anti-CD38 therapy. A significant decrease in IRDye800 fluorescence intensities was observed between treated and untreated cohorts *in vivo* following DARA treatment and imaging with DARA-IR. BLI and *ex vivo* imaging of tumor and non-tumor tissue in the IRDye800 and GFP fluorescent channels confirmed our *in vivo* imaging results. Biodistribution of DARA-IR showed no significant difference in uptake in other non-medullar tissue, suggesting that clearance was not altered due to DARA therapy between untreated and treated mice. *Ex vivo* flow cytometry on excised bone marrow showed significant decrease in MFIs of DARA-IR and no significant difference in MFIs with the commercial CD38 antibody. CD38 receptor was available on myeloma tumors and binding of DARA-IR to CD38 was not altered after multiple

doses of DARA therapy, demonstrating that DARA-IR is a promising tool for noninvasive, preclinical evaluation of CD38 expression in medullar myeloma.

While we anticipated that the therapeutic DARA and DARA-IR would bind to the same epitope of CD38 and observe a subsequent decrease in expression levels following DARA therapy [22], this is not the case for other CD38 mAbs. Isatuximab, another CD38-targeting mAb, binds to different amino acid groups on the CD38 receptor, leading to differences in physical binding to CD38 and a distinct MoA [80]. Continuous exposure to effective concentrations of isatuximab, unlike DARA, does not induce release of CD38 following binding on MM cells [81]. Future studies will focus on evaluating DARA-IR in immunocompetent MM mice in the presence of DARA and other anti-CD38 therapies such as isatuximab. While immunocompromised mice injected with human MM cells are routinely used to test novel imaging agents and therapeutics [94], we recognize that such models do not fully recapitulate the microenvironmental interactions with MM tumors. Further studies investigating DARA-IR uptake in relation to structural and functional markers of the bone marrow microenvironment *in vivo* are warranted.

2.6 Conclusion

Our studies establish DARA-IR as a promising contrast agent for evaluating CD38 expression and activity in medullar MM, and can be used to further investigate myeloma engraftment, progression and kinetics. This agent may lead to better understanding of the MoA of novel CD38-targeted immunotherapies under investigation in animal models of MM and other hematologic malignancies. These future studies can help in developing novel therapy regiments to enhance response and overcome resistance in the treatment of these cancers.

Chapter 3: Tissue Biodistribution and Tumor Targeting of Near-Infrared Labelled Anti-CD38 Antibody Drug Conjugate in Preclinical MM

3.1 Overview

Despite the well-established clinical efficacy of DARA, not all heavily pretreated patients respond to single-agent DARA, and the majority of patients who initially respond eventually progress. Antibody-drug conjugates (ADCs) combine the highly targeted tumor antigen recognition of antibodies with the cell killing properties of chemotherapy for effective internalization and processing of the drug. In this study, we evaluated the anti-tumor efficacy of DARA conjugated to the maytansine derivative, mertansine (DM1), linked *via* a non-cleavable bifunctional linker. The ADC was labelled with the NIR fluorophore IRDye800 (DARA-DM1-IR) to evaluate its stability, biodistribution and pharmacokinetics *in vitro* and *in vivo*. We demonstrated the conjugation of: 1) DM1 enhanced tumor-killing efficacy of the native DARA and 2) IRDye800 allowed for visualization of uptake and tumor targeting ability of the ADC. With the advent of other classes of immunoconjugates for use in MM, we reasoned that such imaging techniques can be utilized to evaluate other promising conjugates in preclinical MM models on a whole-body and cellular level. The material covered in this chapter has been accepted for publication in the journal *Oncotarget*.

3.2 Introduction

DARA is a human IgG1 monoclonal antibody that targets CD38, inducing tumor cell death through multiple mechanisms, including antibody-dependent cell-mediated cytotoxicity (ADCC), complement-dependent cytotoxicity, and antibody-dependent cellular phagocytosis (ADCP) [95]. Despite the well-established clinical efficacy of DARA in RRMM patients, not all

of the heavily pretreated patients respond to single-agent DARA therapy, and the majority of patients who initially respond eventually progress [96]. This may be due to upregulation of pathways that inhibit DARA-mediated ADCC and CDC [22]. One possibility for enhancing the potency of DARA and increasing its therapeutic index is to introduce additional drugs to complement the multiple mechanisms of action of the native immunotherapy. Antibody-drug conjugates (ADCs) combine the highly targeted tumor antigen recognition of antibodies with the cell killing properties of chemotherapy for effective internalization and processing of the drug. The ADC is designed to provide a wider therapeutic window than the antibody alone or the parent cytotoxic drug payload attached to it. Drugs such as maytansines are potent tubulin inhibitors that have previously failed FDA approval due to their poor therapeutic window and lack of tumor specificity, but have demonstrated excellent stability and acceptable solubility in aqueous solutions for use in other clinically-approved ADCs [40]. In this study, we evaluated the anti-tumor efficacy of DARA conjugated to the maytansine derivative, mertansine (DM1), linked *via* the non-cleavable bifunctional linker succinimidyl 4-(N-maleimidomethyl)cyclohexane-1-carboxylate (SMCC) (DARA-DM1). The SMCC linker contains a thioether bond, requiring complete lysosomal degradation of the ADC for intracellular release of the payload, and has demonstrated improved *in vivo* stability and reduced off-target toxicity compared to ADCs with cleavable linkers [35]. The cleaved drug product, lysine-SMCC-DM1, contains a net positive charge, allowing for improved retention in the target cell following internalization of the ADC and reduced off-target toxicities from bystander killing [47]. We posit that DARA conjugated to DM1 *via* a non-cleavable linker will enhance the potency of the native DARA while maintaining high MM tumor specificity and *in vivo* stability.

Binding and internalization of an ADC play critical roles in a biologic's overall

therapeutic potential and delivery of the cytotoxic drug to the target tumor cell. Molecular imaging can serve as a powerful tool to evaluate uptake of antibody-based therapies and provide significant insights into designing next-generation therapeutic agents with superior safety and efficacy. Traditionally, such imaging studies are performed through imaging of radiolabeled compounds with PET or SPECT. While both modalities are highly sensitive and can be used to measure tracer uptake into tissues, the use of decaying radioisotopes and ability to trace just one molecular species (in the case of PET) in a given imaging experiment does not allow for longitudinal monitoring of interactions between molecular targets [85]. Labelling with fluorescent probes for optical imaging in the first near-infrared (NIR-I) window (650nm - 950nm) allows for reduced autofluorescence *in vivo* than in the visible fluorescence range (400 nm - 650 nm) on a whole-body and cellular level in preclinical animal models [86]. While there have been preclinical efforts in developing fluorescently-labelled ADCs for solid cancers [58, 59], there are no published studies evaluating fluorescently-labelled ADCs in preclinical models of MM or other hematologic malignancies.

Here, we labelled DARA-DM1 with the NIR fluorophore IRDye800 (Ex./Em. 774nm/810nm) (DARA-DM1-IR). In addition to efficacy, we evaluated specificity of the ADC, in relation to the native antibody, to myeloma tumor cells both *in vitro* and *in vivo*. We hypothesize that: 1) the conjugation of the drug will enhance the therapeutic efficacy of DARA without affecting tumor targeting of the DARA antibody and 2) labelling with the NIR fluorophore will allow for visualization of DARA-DM1 on a whole-body and cellular level. The proof of principle studies in this article demonstrated the potential of NIR fluorescence imaging for evaluating the cellular uptake and biodistribution of antibody-based therapies in preclinical MM and other hematologic cancers.

3.3 Materials and Methods

3.3.1 *Maytansinoid and fluorophore conjugation of DARA*

Daratumumab (Darzalex, Janssen) was generously donated by the Centre of Advanced Medicine pharmacy, Washington University in St. Louis. DARA-DM1 was synthesized through a one-step reaction. The non-cleavable linker, SMCC, conjugated to DM1 (MedKoo Biosciences) was conjugated to DARA *via* one-step N-hydroxysuccinimide ester reaction at an antibody concentration of 2.5 mg/mL in 1X PBS for 2 hours. A DAR of 20 to 1 was used for conjugation. Unconjugated drug was removed by desalting Zeba spin columns (Thermo Fisher). The final DAR of DARA-DM1 was calculated to be 3.2 *via* mass spectrometry. DARA, DARA-DM1 and non-specific IgG (Sigma Aldrich) were then conjugated to the NIR dye, IRDye800 (Li Cor Biosciences), according to the manufacturer's instructions. Briefly, antibodies were reacted at an antibody concentration of 2.5 mg/mL in 0.1M potassium phosphate buffer (pH 8.5) for 2 hours. Dye to antibody molar ratio of 3 to 1 was used. Unconjugated dye was also removed by desalting Zeba spin columns. The DOL was determined using the DU-640B spectrophotometer (Beckman Coulter) to measure fluorophore absorbance at 774nm and antibody absorbance at 280nm, corrected for the fluorophore. The DOL is defined as the average dye to protein concentration ratio. Fluorescence emission was measured using the Fluorolog-3 spectrofluorometer (Horiba). After purification, conjugates were run on sodium dodecyl sulfate-polyacrylamide gel electrophoresis (SDS-PAGE) (Bio-Rad) in the presence of 1X PBS and human serum (Sigma Aldrich) at 37°C at incubation intervals of 1, 5 and 7 days. Gels were scanned using the Odyssey CLx (Li Cor) measured at 800 nm channel, and images were analyzed in Li Cor Image Studio version 5.2 software.

3.3.2 *Cell Culture*

The human myeloma MM.1S and U266 cells were obtained from ATCC. MM.1S cells were modified to express GFP and click beetle red luciferase (MM.1S-GFP-luc) by the DiPersio laboratory (Professor John F. DiPersio, Department of Medicine, Washington University School of Medicine, St Louis, USA) in 2014. Cells were tested negative for *mycoplasma* by the Washington University Genome Engineering and induced Pluripotent Stem Cell Core *via* MycoAlert PLUS Mycoplasma Detection Kit (Lonza) in 2014 and 2018. All cell lines were passaged 4-5 times following thaw before use in *in vitro* and *in vivo* studies. Cells were cultured in Roswell Park Memorial Institute (RPMI) 1640 medium (Thermo Fisher Scientific) supplemented with 10% heat inactivated fetal bovine serum (FBS) (Sigma Aldrich) and 1% penicillin/streptomycin (Inveon) at 37°C in a humidified environment with 5% CO_2.

3.3.3 *Cytotoxicity studies*

The *in vitro* activity of DARA conjugates was tested using the CellTiter 96 AQueous One Solution Cell Proliferation Assay (Promega) on MM.1S and U266 cells plated at 2.5 x 10^4 cells per well in 96-well round-bottomed plates in triplicate and exposed to ADCs at different concentrations (0 – 10 µg/mL) for 72 hours. IC_{50} values for ADCs were calculated with GraphPad Prism Version 9.1.0 software.

3.3.4 *Cell uptake and internalization studies*

MM.1S and U266 cells were incubated with 75 µg/mL of DARA-DM1-IR in 1X PBS for 1 hour. Cells were then washed twice in fluorescence activated cell sorting (FACS) buffer (made with 1X PBS, 0.5M Ethylenediaminetetraacetic acid disodium salt dihydrate (EDTA) (Corning) and 0.5% Bovine Serum Albumin (Inveon)). Non-specific binding was determined by incubating cells in the presence of excess (50-fold) unlabeled DARA for 1 hour before incubating with

DARA-DM1-IR. Cells were immediately analyzed on the LSR Fortessa (BD).

To evaluate the lysosomal uptake of the DARA conjugates, MM.1S and U266 cells were incubated with 75 µg/mL of DARA-DM1-IR and DARA-IR, respectively, for 3 hours. Cells were washed twice in 1X PBS and fixed and permeabilized with CytoFAST Fix and Perm buffer (BioLegend). Cells were then stained with PE anti-human CD107a (LAMP-1) antibody (BioLegend) in the dark for 30 minutes. Cells were washed twice in FACS buffer and immediately analyzed on the LSR Fortessa. 7-aminoactinomycin D (Thermo Fisher Scientific) $(7AAD)^-$ population was considered as viable tumor cells and used for statistical analysis for both studies. PE mouse anti-human CD38 (BD) was used to evaluate CD38 expression on MM.1S and U266 cells. Blue laser (Ex. 488 nm) was used to detect 7AAD (Em. 695/40 nm), yellow laser (Ex. 552 nm) was used to detect PE (Em. 585/15 nm) while red laser (Ex. 640 nm) was used to detect IRDye800 (Em. 780/60 nm). Flow cytometry data was analyzed with FlowJo Version 10.6.2 software.

3.3.5 *Live cell microscopy*

300,000 MM.1S-GFP-luc cells/mL were seeded into 6-well tissue culture-treated plates (Corning) and incubated with 150 µg/mL of DARA-IR and DARA-DM1-IR at 37°C for 3 hours in 1X PBS. Cells were then washed twice in 1X PBS and immediately imaged on Cell Discoverer 7 (Zeiss) in the GFP (Ex./Em. 465nm/520nm) and Cy5 (Ex./Em. 640nm/680nm) wavelength channels with a 20X objective. Microscopy images were acquired with ZEN 3.2 (blue edition) software (Zeiss) and exported to and analyzed with NIH Image J software.

3.3.6 *Animal models*

All animal studies were performed in accordance with the Institutional Animal and Use Committee of Washington University School of Medicine. Mice were anesthetized for all

treatments and imaged with 2% v/v isoflurane/100% O_2. Female 1-3 month old fox chase SCID mice (Charles Rivers Laboratories) were injected with $3*10^6$ MM.1S-GFP-luc cells in 100µL 1X PBS SQ or IV *via* lateral tail vein. Tumor burden was monitored weekly *via* BLI prior to administration of DARA conjugates in both mouse models. For imaging studies in MM.1S SQ and IV mice, mice were randomized into respective cohorts when a mean bioluminescence flux of $1*10^9$ photons/second was achieved.

3.3.7 *In vivo therapy studies*

Weekly BLI was performed on MM.1S IV mice until they reached a mean bioluminescence flux of $6*10^6$ photons/second. Mice were then randomized into untreated and treated cohorts (n=6-7/group). Treated mice were provided DARA and DARA-DM1 IP at a single dose of 4 mg/kg of body weight in 1X PBS. Additional BLI was performed twice per week to measure tumor cell viability for 6-7 weeks.

3.3.8 *In vivo and ex vivo fluorescence imaging studies*

DARA-DM1-IR and DARA-IR, respectively, was administered IV in 1X PBS at 4 mg/kg of body weight in MM.1S SQ and MM.1S IV mice (n = 3-4/group). For MM.1S SQ mice, daily optical imaging in the GFP (Ex./Em. 480nm/535nm) and IRDye800 channels (Ex./Em. 785nm/820nm) was performed up to 9 days following injection using the IVIS Spectrum CT (Perkin Elmer). For MM.1S IV mice, optical imaging in the GFP (Ex./Em. 480nm/535nm) and IRDye800 channels (Ex./Em. 785nm/820nm) was performed 9 days following injection using the Optix MX3 time-domain diffuse optical imaging system. Prior to imaging, hair was removed by gentle clipping and depilatory cream to improve light transmission. Following imaging, mice were sacrificed at appropriate time points and tissue was excised. GFP (Ex./Em. 480nm/535nm) and IRDye800 (Ex./Em. 780nm/820nm) fluorescent images of excised tissue were acquired on

the IVIS Spectrum CT (Perkin Elmer), respectively. TBRs were calculated from IRDye800 fluorescent images of MM.1S SQ mice by drawing equivalently-sized ROIs in NIH ImageJ software around GFP^+ tumor-bearing regions and non-fluorescent (background) regions on the contralateral side of the mouse and measuring total radiant efficiency (TRE). TMRs in *ex vivo* GFP and IRDye800 fluorescent images were calculated in Perkin Elmer Living Image 4.7.1 software. Analysis of *ex vivo* fluorescent images was performed by measuring TRE from ROIs drawn around bone and muscle tissue. TMRs were calculated by dividing TREs of tissue by TREs of muscle tissue of each respective mouse.

3.3.9 *Fluorescence immunohistochemistry*

MM.1S SQ mice were euthanized 9 days post-administration of DARA-IR and DARA-DM1-IR and tumors were resected, flash frozen in Tissue-Tek optimal cutting temperature (OCT) compound (Sakura) at -80°C and cut for histology on a cryostat (5-µm slices). Slices were stained with Hoechst 33342 (Fisher Scientific) and microscopy was performed using an upright Olympus BX51microscope (Olympus) equipped with a 40X objective and 405, 488 and 745nm lasers. Tumor images were collected with Olympus Cells Standard 1.6 software and exported into NIH ImageJ software for analysis.

3.3.10 *Ex vivo flow cytometry*

Viable cells were obtained from tibial and femoral bone marrow flush from MM.1S IV mice, washed in FACS buffer, stained and immediately analyzed with LSR Fortessa. For GFP^+ tumor graft viability, $7AAD^-/GFP^+$ population was considered as viable tumor cells and lasers were used as previously described. Blue laser (Ex. 488nm) was used to detect FITC (Em. 530/30nm). Binding of DARA-IR and DARA-DM1-IR to MM cells in the bone marrow was

assessed using MFIs of IRDye800. Flow cytometry data was analyzed with FlowJo Version 10.6.2 software as previously described.

3.3.11 *Statistical analysis*

All data is presented as mean ± standard deviation and statistical analysis was performed using GraphPad Prism Version 9.1.0 software. Statistical significance between cohorts was calculated using Student t-test and one-/two-way analysis of variance (ANOVA) followed by Sidak's multiple comparisons test, unless specified otherwise. P values of less than 0.05 were considered statistically significant.

3.4 Results

3.4.1 *Synthesis and characterization of DARA-DM1 and DARA-DM1-IR*

DM1 was conjugated to DARA at a molar ratio of 20 to 1. Mass spectrometry was performed on DARA-DM1 to calculate a DAR of 3.2 with less than 10% of unconjugated DARA remaining following DM1 conjugation (Figure 3.1A). Following DM1 conjugation, IRDye800 was labelled to DARA-DM1 and DARA at a dye to antibody ratio of 3 to 1. Absorption spectroscopy showed a similar DOL of IRDye800 to both DARA-DM1 and DARA at ~1.3-1.4 (Figure 3.1B). Fluorescence spectroscopy confirmed that there was not a difference in brightness between the two conjugates (Figure 3.1C).

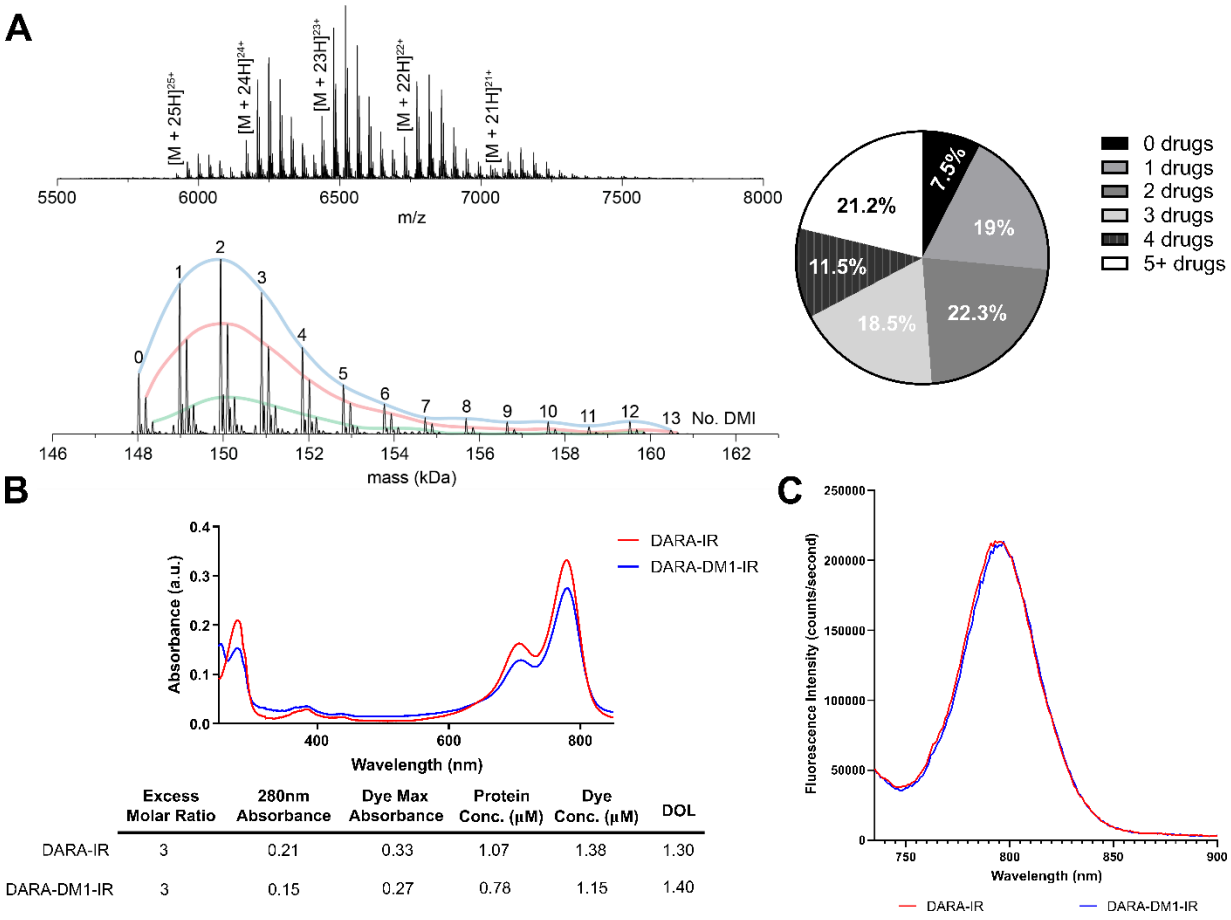

	Excess Molar Ratio	280nm Absorbance	Dye Max Absorbance	Protein Conc. (µM)	Dye Conc. (µM)	DOL
DARA-IR	3	0.21	0.33	1.07	1.38	1.30
DARA-DM1-IR	3	0.15	0.27	0.78	1.15	1.40

Figure 3.1: Analytical characterization of DARA-DM1 and DARA-DM1-IR. A) Representative mass spectrometry spectra and percent distribution of DARA with 1, 2, 3, 4 or 5+ DM1 drugs per antibody at a 20 to 1 conjugation ratio. B) Antibody-dye absorbance spectra of DARA-DM1-IR and DARA-IR. After reaction and purification, the absorbance spectrum for DARA-DM1-IR and DARA-IR were used to determine the DoL as described in the methods section. DoL was determined by dividing bulk fluorophore concentration by antibody concentration. C) Fluorescence emission spectra of DARA-DM1-IR and DARA-IR.

3.4.2 *Cytotoxicity of DARA-DM1 and DARA-DM1-IR*

To evaluate the *in vitro* cytotoxicity of DARA-DM1 compared to the native DARA antibody, DARA conjugates were incubated with two human myeloma cell lines, MM.1S and

U266, in a dose-dependent fashion. CD38 expression was evaluated on both cell lines *via* flow cytometry showing high and low expression of CD38 on MM.1S and U266 cell lines, respectively (Figure 3.2A). DARA-DM1 and DARA-DM1-IR both exhibited a statistically significant difference in cytotoxicity in MM.1S cells (DARA-DM1 IC_{50}: 0.43 $\pm$ 0.05 µg/mL; DARA-DM1-IR IC_{50}: 0.40 $\pm$ 0.03 µg/mL) compared to U266 cells (DARA-DM1 IC_{50}: 2.54 $\pm$ 0.4 µg/mL; DARA-DM1-IR IC_{50}: 4.58 $\pm$ 0.7 µg/mL) ($p < 0.0001$). Conjugation of IRDye800 to DARA-DM1 did not show a statistical difference in tumor-killing ability when compared to DARA-DM1 in MM.1S cells, but showed a statistical difference in U266 cells ($p < 0.0001$) (Figure 3.2B).

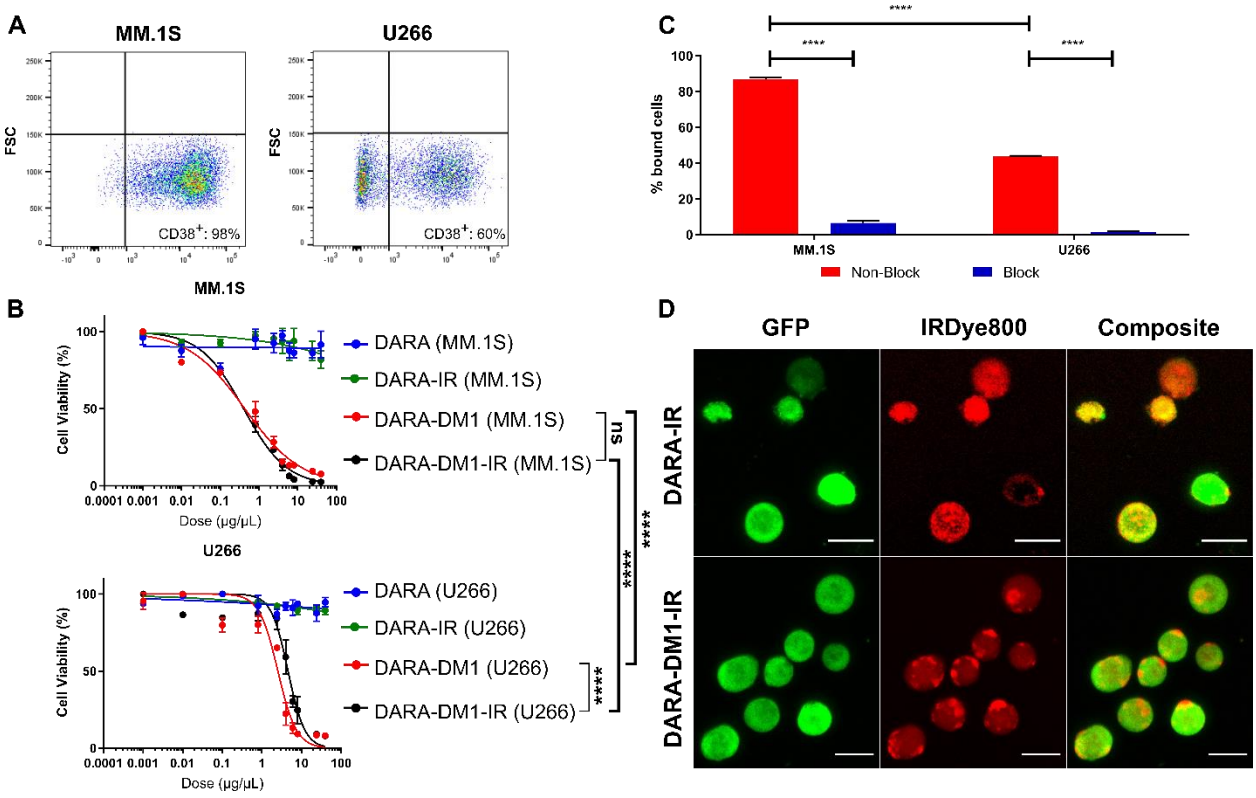

Figure 3.2: *In vitro* evaluation of cytotoxicity, binding and internalization of DARA-DM1-IR A) Flow cytometric evaluation of CD38 expression in human MM.1S and U266 myeloma cells. B) Comparison of cytotoxicity of DARA-DM1 and DARA-DM1-IR and control DARA

and DARA-IR in human MM.1S and U266 myeloma cells. All experiments were performed in triplicate and repeated twice. Two-way ANOVA followed by Sidak's multiple comparison's test was performed on IC_{50} values. C) Percentage cell binding of DARA-DM1-IR in MM.1S and U266 cells at 37°C in the absence and presence of 50-fold blocking dose of unlabeled DARA. Two-way ANOVA followed by Sidak's multiple comparison's test was performed. D) Live cell fluorescence microscopy of internalization of DARA-IR and DARA-DM1-IR in MM.1S-GFP-luc cells 3 hours post-incubation. Magnification: 20X; Scale bar: 20µm; ****$p < 0.0001$. Error bars represent standard deviation.

3.4.3 *Evaluation of stability, binding and internalization properties of IRDye800-conjugated antibodies*

Stability of DARA-IR and DARA-DM1-IR in PBS and human serum was measured over 7 days. Both IRDye800 conjugates maintained > 80% NIR signal by day 7, indicating minimal dye deconjugation and formation of free dye during incubation (Figure 3.3).

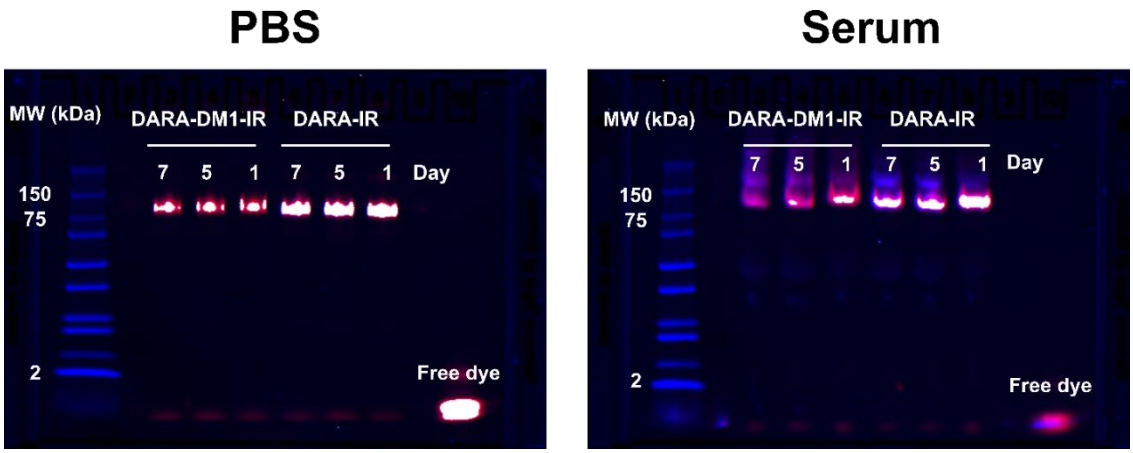

Figure 3.3: In vitro stability of DARA-DM1-IR and DARA-IR. SDS-PAGE of DARA-DM1-IR and DARA-IR incubated in PBS and human serum between 1 and 7 days.

Flow cytometry and fluorescence microscopy were performed to determine if conjugation of IRDye800 to the ADC perturbed the antibody's binding property. DARA-DM1-IR demonstrated significant binding in MM.1S and U266 cells in a CD38-dependent manner (MM.1S: 86.8 ± 0.9%; U266: 43.6 ± 0.4%). Blocking of CD38 receptor with excess DARA demonstrated significantly reduced binding of DARA-DM1-IR in both cell lines (MM.1S: 6.46 ± 1.1%; U266: 1.53 ± 0.5%) (Figure 3.3C). Evaluation by flow cytometry of the lysosomal-associated membrane protein 1 (LAMP-1) staining in MM.1S and U266 cells corresponded with binding, showing significant intracellular internalization of both DARA conjugates in MM.1S cells (DARA-IR: 96.2 ± 0.3%; DARA-DM1-IR: 98.5 ± 0.1%), but significantly reduced internalization in U266 cells (DARA-IR: 12.7 ± 0.7 %; DARA-DM1-IR: 12.2 ± 1.8%) (Figure 3.4).

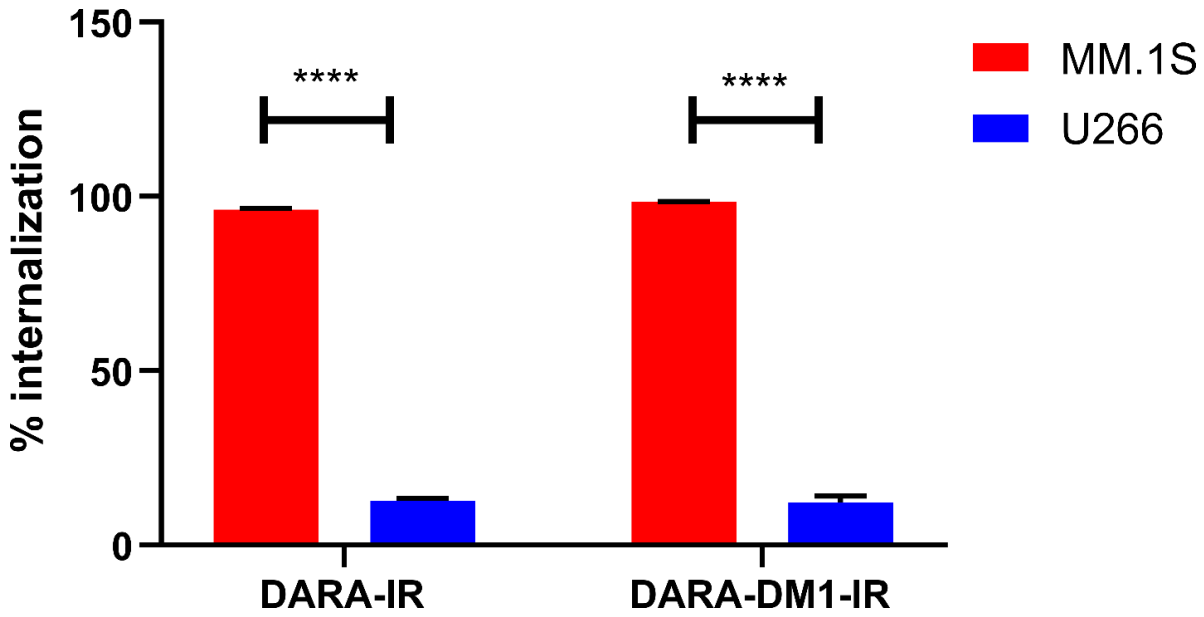

Figure 3.4: Internalization of DARA conjugates. Flow cytometric analysis of percent of MM.1S and U266 cells internalized with DARA-IR and DARA-DM1-IR in LAMP-1^{+} lysosomes

3 hours post-incubation. Student t-tests were performed for each conjugate and cell line. ****$p < 0.0001$. Error bars represent standard deviation.

Fluorescence microscopy of MM.1S cells incubated with both DARA conjugates validated flow cytometric LAMP-1 staining results, showing significant internalization within 3 hours (Figure 3.3D).

3.4.4 *In vivo therapeutic efficacy of DARA-DM1*

To demonstrate the therapeutic efficacy of DARA-DM1 *in vivo*, fox chase severe combined immunodeficient (SCID) beige mice injected intravenously (IV) with MM.1S cells transfected with green fluorescence protein (GFP) and luciferase (MM.1S IV) were treated with either DARA or DARA-DM1 at doses of 4mg/kg of body weight and were monitored with bioluminescence imaging (BLI). DARA-DM1 resulted in significant tumor eradication following single administration of DARA-DM1. While the unconjugated DARA also demonstrated significant activity in mice at a single dose, mice still observed some tumor burden by the end of the study (Figure 3.5A). No significant weight loss was demonstrated in any of the untreated or treated (DARA and DARA-DM1) mice. *Ex vivo* flow cytometry on excised femoral and pelvic bone marrow, gating for live, GFP^+ tumor cells, verified the anti-MM effect seen with *in vivo* BLI results (Figure 3.5B).

A

Day	14	18	21	25	28	33	36	39	43
Untreated versus DARA Treated	ns	ns	ns	ns	ns	*	**	***	****
Untreated versus DARA-DM1-treated	****	***	**	**	*	**	**	***	****
DARA treated versus DARA-DM1 treated	****	ns	ns	ns	ns	ns	ns	ns	ns

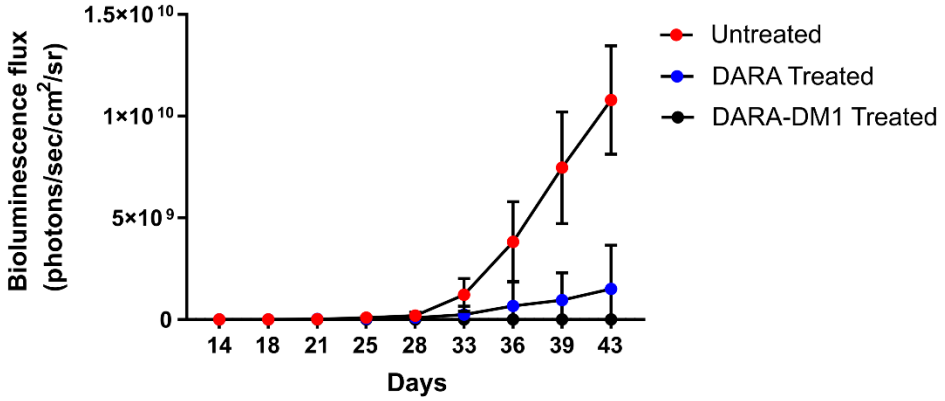

B

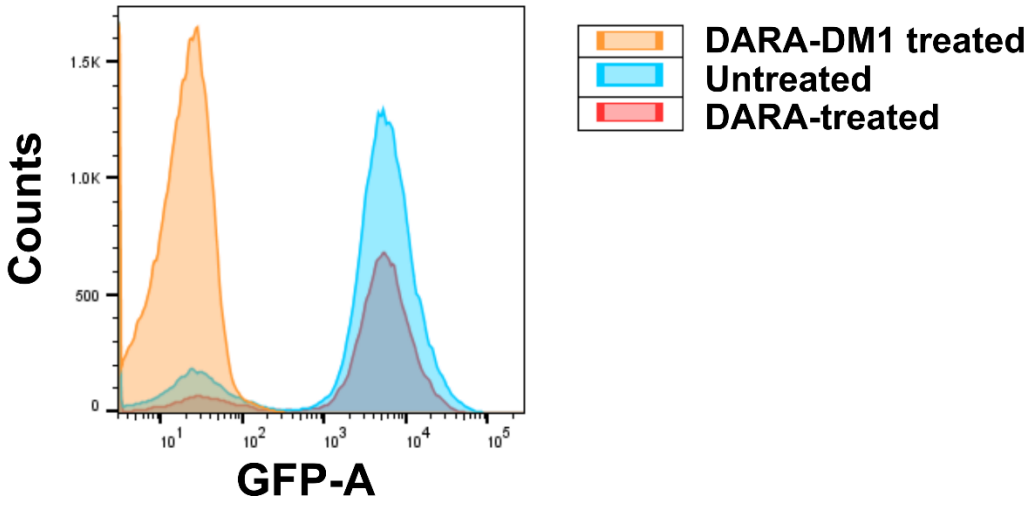

Figure 3.5: In vivo therapeutic efficacy of DARA-DM1 in intramedullar myeloma mice A) Longitudinal BLI of MM.1S IV mice treated with a single dose of DARA or DARA-DM1 measured as bioluminescence flux (photons/sec/cm^2/sr). n=6-7/group. Repeated measures two-way ANOVA followed by Sidak's multiple comparison's test was performed. B) Representative flow cytometry from excised bone marrow of untreated and treated mice, gating for live, GFP$^+$

MM cells. *$p < 0.05$; **$p < 0.01$; ***$p < 0.001$; ****$p < 0.0001$. Error bars represent standard deviation.

3.4.5 *High specificity of DARA-DM1-IR to CD38$^+$ myeloma extramedullary tumors*

To quantify contrast and the optimal imaging time point of DARA-DM1-IR, SCID beige mice bearing subcutaneous (SQ) tumor xenografts (MM.1S SQ) were injected IV with the fluorescent conjugate. Significant uptake of DARA-DM1-IR was observed in GFP$^+$ tumor-bearing regions by day 9 of fluorescent imaging (Figure 3.6A). Region of Interest (ROI) analysis of small-animal fluorescent imaging with DARA-DM1-IR showed high contrast, calculated as Tumor to Background Ratio (TBR), at later time points, reaching a peak of 3.3 ± 0.4 at day 9 as compared to a TBR of 4.0 ± 0.7 in mice injected with DARA-IR (Figure 3.6B). This optimal time point informed the imaging in studies involving the MM.1S IV mouse model. A statistically significant difference in TBRs between DARA-DM1-IR and DARA-IR was observed at Day 8 ($p < 0.01$) and 9 ($p < 0.05$). Tissue biodistribution studies performed in the IRDye800 channels at 2, 7 and 9 days post-administration of DARA-DM1-IR and DARA-IR were in agreement with the *in vivo* fluorescent imaging data, calculated as Tissue to Muscle Ratio (TMR), showing high uptake and retention of the fluorescent conjugate 9 days after injection (DARA-DM1-IR TMR: 13.9 ± 2.6; DARA-IR TMR: 15.5 ± 4.8) (Figure 3.6C). Significant differences in non-tumor tissue were observed primarily in the liver with greater uptake of DARA-DM1-IR at day 2 (DARA-DM1-IR TMR: 50.6 ± 17.1; DARA-IR TMR: 22.8 ± 4.2) and day 7 (DARA-DM1-IR TMR: 19.2 ± 2.6; DARA-IR TMR: 14.2 ± 2.2) (Figure 3.6C). Similar liver uptake was observed between the two antibody conjugates by day 9 (DARA-DM1-IR TMR: 12.2 ± 0.9; DARA-IR TMR: 11.9 ± 1.6). Immunofluorescence staining of excised tumors supported *in vivo* and *ex vivo*

imaging results and demonstrated specific binding of DARA-DM1-IR, similarly to DARA-IR, to tumor cells (Figure 3.6D).

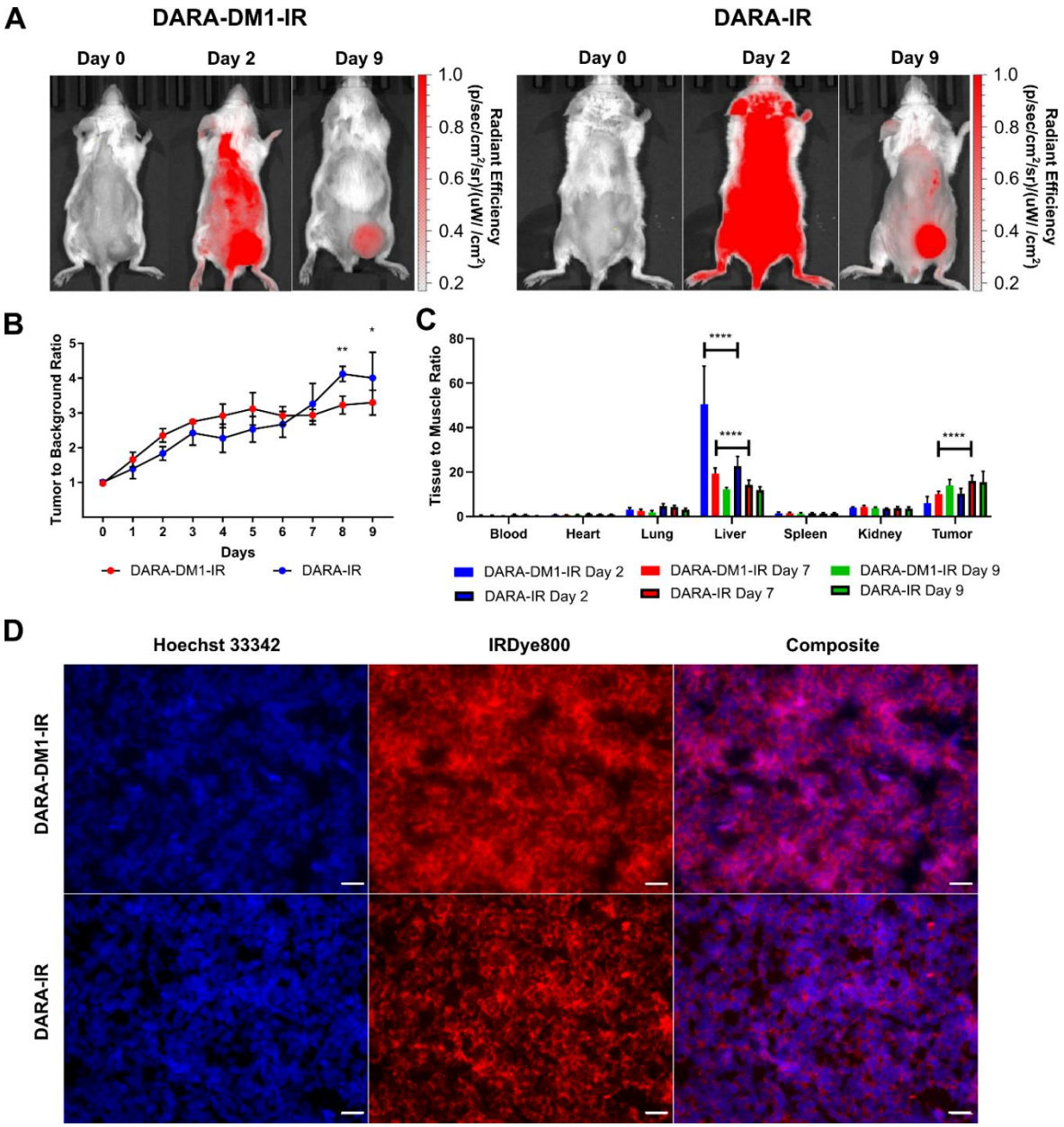

Figure 3.6: High contrast observed with DARA-DM1-IR at longer time points in MM.1S SQ mice. A) Representative IRDye800 in vivo images of MM.1S SQ mice 2 and 9 days post administration of DARA-DM1-IR and DARA-IR. B) Plot of calculated TBRs in MM.1S SQ mice across individual time points following administration of DARA-DM1-IR and DARA-IR.

Background is defined as the non-tumor, contralateral left flank of the mouse. Repeated measures two-way ANOVA followed by Sidak's multiple comparison's test was performed on TBR data. n = 3-4/group. C) Normalized biodistribution (defined as tissue to muscle ratio (TMR)) of DARA-DM1-IR 2,7 and 9 days after administration of fluorescent conjugate. n = 3-4/group. Two-way ANOVA followed by Sidak's multiple comparisons test was performed on biodistribution data. D) Immunohistochemistry of excised tumor sections from mice injected with DARA-DM1-IR and DARA-IR. Nuclear stain was performed with Hoechst 33342. Magnification: 40X; Scale bar: 100µm; * $p < 0.05$; ** $p < 0.01$; **** $p < 0.0001$. Error bars represent standard deviation.

3.4.6 *High specificity of DARA-DM1-IR to CD38$^+$ myeloma intramedullary tumors*

In vivo fluorescent imaging of DARA-DM1-IR was also performed in the MM.1S IV mouse model. Similar to the SQ mouse model, DARA-DM1-IR showed specificity to GFP$^+$ tumors in marrow-rich regions such as the skull, long bones and spine (Figure 3.7A,B) 9 days post-administration. Tissue biodistribution studies in tumor and non-tumor tissue from mice injected with DARA-DM1-IR and DARA-IR, respectively, showed similar uptake of both conjugates in bone regions (DARA-DM1-IR TMR: 20.4 $\pm$ 7.2; DARA-IR TMR: 18.4 $\pm$ 2.2) and greater uptake than in bones from mice injected with a non-specific IgG-IR (IgG-IR TMR: 8.2 $\pm$ 1.1).

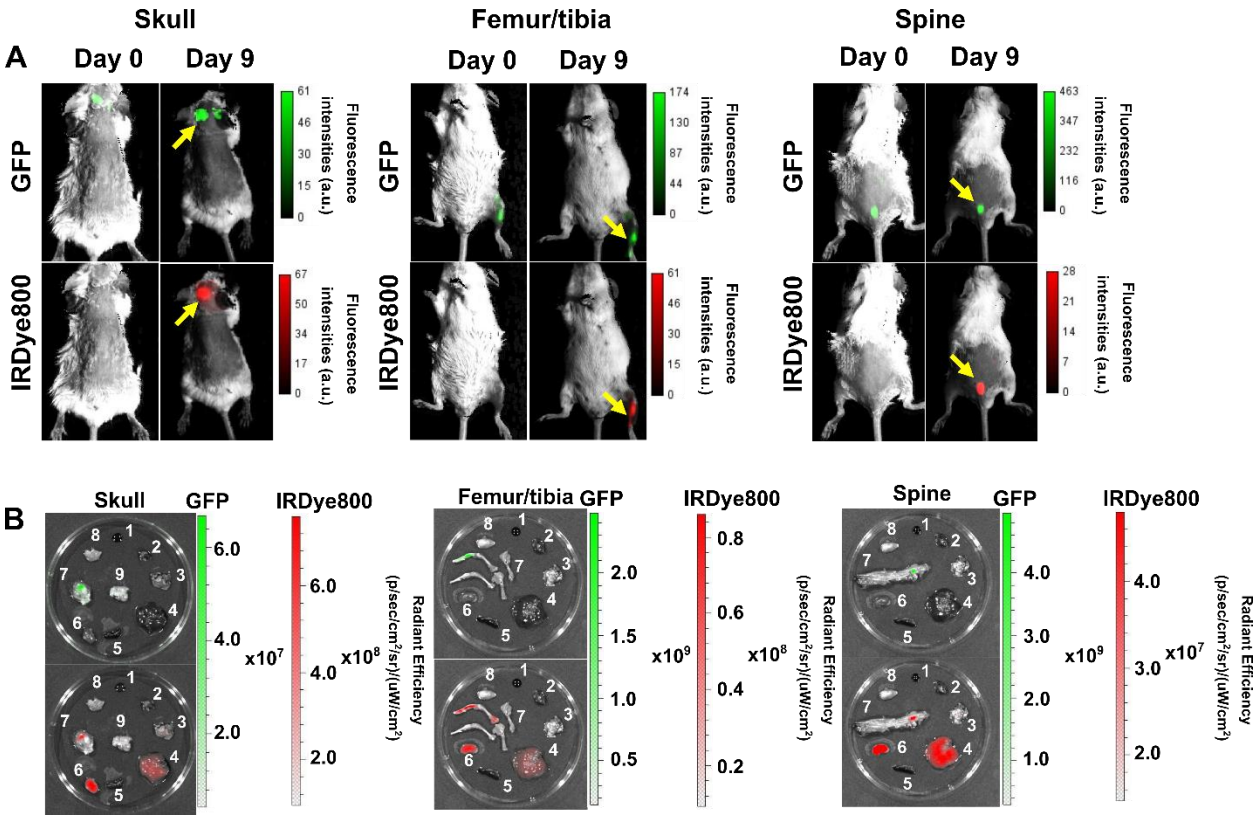

Figure 3.7: Specific binding of DARA-DM1-IR to cancerous bone marrow regions in MM.1S IV mice. A) Representative images of GFP and IRDye800 fluorescence in vivo of skull, long bones and spine (yellow arrows) in separate MM.1S IV models 9 days post administration of DARA-DM1-IR. B) Representative GFP and IRDye800 fluorescent images of excised 1) blood 2) heart 3) lung 4) liver 5) spleen 6) kidney 7) bone 8) muscle 9) brain from mice. a.u.: arbitrary units.

Liver uptake of DARA-DM1-IR (TMR: 43.3 ± 15.4) was similar to IgG-IR (TMR: 43.8 ± 6.6) and was higher than the uptake of DARA-IR (TMR: 23.0 ± 7.6) (Figure 3.8A). Flow cytometry on the excised bone marrow, measured as mean fluorescence intensities (MFI), confirmed *in vivo* and *ex vivo* images and showed significantly increased uptake of DARA-DM1-IR (MFI: 9832 ± 1545) and DARA-IR (MFI: 11715 ± 3475) relative to IgG-IR (MFI: 319

± 86.75) with no significant difference between uptake of DARA-DM1-IR and DARA-IR (Figure 3.8B).

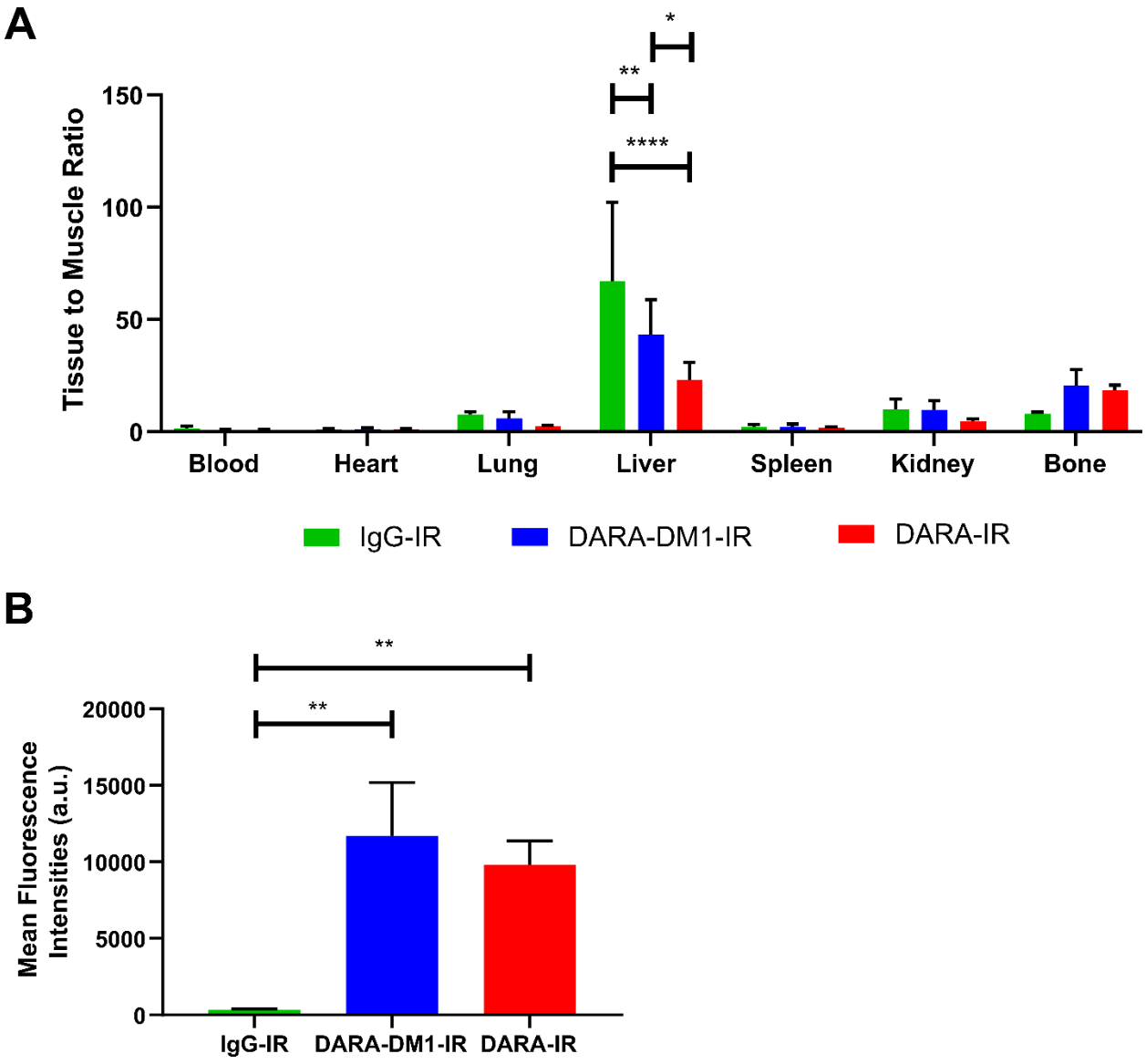

Figure 3.8: Biodistribution and flow cytometric analysis of DARA-DM1-IR in MM.1S IV mice. A) Normalized biodistribution (defined as TMR) of DARA-DM1-IR, DARA-IR and IgG-IR 9 days after administration of fluorescent conjugate. n = 3-4/group. Two-way ANOVA followed by Sidak's multiple comparisons test was performed on biodistribution data. B) Flow cytometric analysis of IRDye800 MFIs from excised bone marrow of DARA-DM1-IR, DARA-

IR and IgG-IR-injected mice. One-way ANOVA followed by Tukey's multiple comparisons test was performed on flow cytometry data. n = 3-4/group. *p < 0.05; **p < 0.01; ***p < 0.001; ****p < 0.0001. Error bars represent standard deviation.

3.5 Discussion

CD38 is highly expressed on MM cells and is involved in their development and proliferation, making CD38 an attractive therapeutic target. DARA was the first Food and Drug Administration (FDA)-approved anti-CD38 immunotherapy prescribed to relapsed and refractory MM patients. While DARA is well tolerated and has robust clinical efficacy, not all heavily pretreated patients respond to single-agent DARA, necessitating other therapeutic agents to overcome this resistance [22, 97]. Several mechanisms have been proposed that are driving DARA resistance, including upregulation of complement inhibitors, clonal selectivity and microenvironmental interactions with bone marrow stromal cells [23]. CD38 expression is excluded as a possible reason, as responders and non-responders of DARA treatment show a marked reduction in CD38 [98]. A highly appealing strategy is to utilize the targeting power of antibodies as carriers of potent effector moieties to the target tumor cell. With the recent success of clinically approved ADCs in MM, such as Blenrep (anti-BCMA) [99], and other ADCs undergoing clinical trial, such as IMGN901 (anti-CD56) [100], both of which rely on delivery of cytotoxic drug payloads with non-cleavable linkers, the potential of ADCs and similar immunoconjugates will be increasingly evaluated in such heavily pretreated MM patients. The general mechanism of cytotoxicity for such immunoconjugates includes binding and subsequent internalization into the cell, cleavage of the linker-drug complex and the release of the payload for killing the target cell [101]. The payloads of the ADCs described previously either damage DNA or impede microtubule assembly while retaining all the mechanisms of action of the native

antibody, introducing an additional mechanism to overcome drug insensitivity [38, 76] . We reasoned that a similar conjugation of a cytotoxic drug to DARA could also widen its therapeutic window.

Here we demonstrate the use of DARA conjugated to the non-cleavable linker SMCC and the maytansinoid DM1 because of the improved *in vivo* stability and reduced bystander killing associated with drug payloads linked *via* non-cleavable linkers [40]. Free DM1 has also shown significant cytotoxicity to MM cells *in vitro* [102]. DARA has demonstrated preferential killing of high CD38-expressing MM cells, allowing for expansion of MM cells with low CD38 ($CD38^{low}$) expression with reduced CDC and ADCC killing [98]. With the immunosuppressive nature of non-responders to DARA therapy [16, 23, 27], we believe the ADC could potentially target and kill $CD38^{low}$ MM cells in the presence of reduced effector cell populations that DARA is reliant upon. We anticipate that DARA-DM1 will allow for a greater percentage of DM1 drug to reach tumors, lowering the minimum effective dose and elevating the maximum tolerated dose of drug payload. To evaluate the binding, internalization and distribution of DARA-DM1, we labelled the ADC with the NIR fluorophore IRDye800. With the advent of anti-CD38 ADCs [103], radiotherapies [104] as well as other classes of immunotoxins for use in MM [76] , the NIR-labelling techniques applied in this manuscript can be used to visualize similar immunoconjugates in preclinical MM models *in vitro* and *in vivo* for more efficient clinical translation in MM.

At a DAR of 3.2, DARA-DM1 was found to have less than 10% DARA remain unconjugated. As expected with lysine-based conjugation, a heterogeneous distribution of 1-5 DM1 molecules was conjugated to DARA. While IRDye800 also requires free lysines for conjugation, preferentially on the heavy chain of the antibody [105, 106], absorbance and

fluorescence spectroscopy demonstrated a similar DOL of ~1.3-1.4 between DARA-DM1-IR and DARA-IR without any differences in fluorescence emission. This suggests that the presence of DM1 and the heterogeneity of lysine conjugation did not inhibit labelling of IRDye800 to the DARA antibody.

Two human MM cell lines, MM.1S and U266, with different levels of CD38 expression were utilized to evaluate the cytotoxicity and mechanism of action of the DARA immunoconjugates. We demonstrated that conjugating DM1 enhanced cytotoxicity of the native DARA in a CD38-dependent fashion. DARA, conversely, did not demonstrate any cytotoxicity in either cell line, likely due to the lack of effector cells for the antibody to induce cell killing. Our flow cytometry and fluorescence microscopy studies showed that these differences in cytotoxicity may be due to differences in binding and internalization of DARA-DM1 in the MM.1S and U266 cells. While DARA-DM1 bound to both cell lines, we showed that there is significantly reduced binding and lysosomal internalization intracellularly in U266 cells than in MM.1S cells, corresponding with reduced CD38 expression and thus requiring greater concentration of DARA-DM1 to induce cytotoxicity. This is consistent with ADCs composed of non-cleavable linkers, which require lysosomal proteolytic degradation of the antibody [45]. These studies, additionally, corroborated that the conjugation of IRDye800 at a DOL of ~1.3-1.4 did not affect the stability or functional properties of DARA or DARA-DM1.

DARA-DM1 demonstrated significant *in vivo* single-dose efficacy within ~ 4 days in MM.1S IV mice compared to the native DARA. While DARA-treated mice showed reduced tumor burden 33 days post-tumor inoculation, DARA-DM1-treated mice showed early and near complete elimination of tumor burden with no weight loss observed in either mouse cohort. DARA monotherapy was likely efficacious *in vivo* due to ADCP activity [107] with the presence

of normal macrophage and granulocyte populations in SCID beige mice [108]. These results demonstrated that, while DARA monotherapy still had significant therapeutic efficacy, conjugation of DM1 to DARA allowed for early and sustained elimination of tumor burden.

DARA-DM1-IR and DARA-IR were imaged in MM.1S SQ and MM.1S IV mice to evaluate the tissue biodistribution and tumor targeting of DARA-DM1 in relation to DARA. Our *in vivo* imaging results showed that both immunoconjugates had high specificity to GFP^+ tumor lesions in both mouse models. We, and others, have previously demonstrated that IV injection of human myeloma cells results in diffuse tumor growth in variable regions of bone marrow in mice compared to the localized tumor burden observed in MM.1S SQ mice [77, 94]. MM is a plasma cell disorder that causes significant skeletal morbidity within the bone marrow niche. As anticipated, both DARA-DM1-IR and DARA-IR uptake was observed in bone marrow regions in the MM.1S IV mice including skull, long bones and spine. Spatial tumor heterogeneity is characteristic of MM and the presence of circulating tumor cells may be contributing to the uptake of MM cells in different bone regions. Differences in the efficiency of tail vein injections of MM.1S cells and mouse-to-mouse variability in cytokines such as IL-6 may additionally be why some mice develop more tumor burden in one region than others. SCID beige mice also have several, normal lymphocyte populations, which may contribute to allogeneic tumor rejection from the host immune system, leading to variability in tumor uptake [108].

Ex vivo biodistribution demonstrated significant clearance through liver by day 9 in MM.1S SQ and IV mice. Due to their large size (~ 150kDa), IgG antibodies such as DARA are primarily catabolized *via* the liver [92]. The greater hepatic uptake of DARA-DM1 relative to native DARA can be attributed to the higher hydrophobicity associated with ADCs, resulting in greater reticuloendothelial system clearance [109, 110]. These differences in liver uptake did not

affect the tumor targeting ability of DARA-DM1, as seen in the *ex vivo* biodistribution as well as fluorescent microscopy and flow cytometry studies on the excised tumor tissue, but may have contributed to the differences in TBR at later time points when compared to DARA in the MM.1S SQ mice. It should be noted that DARA does not bind to murine CD38, therefore, in combination with the lack of a competent immune system, mice are not an ideal species for evaluating the off-target toxicity of the intact humanized ADCs. Future studies in humanized, immunocompetent mouse models of MM that can recapitulate the microenvironmental interactions with MM tumors are warranted.

3.6 Conclusion

Our studies demonstrate that conjugation of DM1 to the native DARA significantly enhanced its therapeutic efficacy *in vitro* and *in vivo*. Fluorophore labelling did not affect the stability or activity of the biologic and showed that both DARA-IR and DARA-DM1-IR had similar binding and biodistribution profiles. These imaging techniques can be applied to other immunotherapies and antibody conjugates under investigation in animal models of diverse hematologic cancers to evaluate similar parameters demonstrated in this article. Future studies can help in mechanistically understanding these therapies to enhance response and overcome resistance in treatment of these cancers.

Chapter 4: Chapter Summary

4.1 Summary

Despite the well-established clinical efficacy of DARA, there are still RRMM patients who do not achieve a partial response and the mechanisms involved in this lack of DARA response are still not entirely clear. The aim of this thesis was to show that the conjugation of a cytotoxic agent could enhance the therapeutic efficacy of the native DARA and could be visualized *via* NIR fluorescence. In the following two specific aims, we rationalized that the imaging techniques demonstrated here can be used to evaluate the mechanisms of action and biodistribution of other novel anti-CD38 biologics on a whole-body and cellular level in preclinical MM.

Aim 1: Develop a fluorescently-conjugated DARA for targeted imaging in preclinical MM

In this study, I conjugated the native DARA with the NIR fluorophore IRDye800CW for monitoring of the antibody and the CD38 receptor *in vivo*. Conjugation of IRDye800 to DARA did not affect the stability or targeting of the native antibody to CD38 on MM cells. DARA-IR demonstrated high specificity to GFP^+ MM cells in mice with intramedullar myeloma with clearance primarily through the liver and spleen. *Ex vivo* flow cytometry on excised BM from mice injected with DARA-IR in relation to a non-specific IgG-IR control validated *in vivo* imaging results.

DARA-IR was also used as a contrast agent to evaluate CD38 expression in mice treated with DARA at a therapeutic dose. DARA-treated mice demonstrated a significant decrease in uptake of DARA-IR compared to untreated mice. *Ex vivo* flow cytometry on BM from mice of both cohorts, stained with a commercial PE anti-CD38, validated *in vivo* binding of DARA-IR to the target receptor. These results demonstrated that DARA-IR can also be used as a tool for non-

invasive, preclinical evaluation of CD38 expression in medullar myeloma.

Aim 2: Enhance cytotoxicity of DARA with DM1 and use fluorescence imaging to visualize uptake and biodistribution of fluorescent ADC

In this aim, I conjugated the maytansinoid, DM1, to DARA to enhance its therapeutic efficacy without affecting its biologic activity. IRDye800 was conjugated to the ADC to evaluate its mechanism of action and biodistribution. DARA-DM1 demonstrated significant single-dose cytotoxicity *in vitro* and *in vivo* in a CD38-dependent manner. DARA-DM1 bound and internalized in lysosomal compartments in MM cells similar to the native DARA. Finally, when imaging both DARA constructs in mice with extra- and intramedullar myeloma, DARA-DM1 showed higher uptake than DARA in liver. *Ex vivo* immunohistochemistry and flow cytometry on tumor tissue validated that, despite these differences in biodistribution, tumor targeting was not affected by conjugation of DM1 and IRDye800 to DARA. The results from this aim proved the utility of NIR fluorescence imaging in evaluating different antibody-based therapies in preclinical MM.

4.2 Limitations

There are certain limitations to the approach in this project. Most aim-specific limitations are addressed in each chapter individually, but general limitations affecting the results of this thesis remain. The primary limitations were the use of a single myeloma cell line and the use of immunocompromised mice for evaluating therapy and imaging. CD38 is expressed on other non-tumor immune cells and DARA has been shown to interact with these cells. Future *in vitro* studies recapitulating the BM microenvironment with human PBMCs and bone marrow stromal cells (BMSCs) from healthy and DARA resistant patients are warranted to evaluate the binding, internalization and cytotoxicity of DARA-IR and DARA-DM1 in these non-tumor cells.

Similarly, while immunocompromised mice used in these studies allowed for evaluation DARA and DARA-DM1's specific interactions with MM tumor cells, DARA also does not bind to murine CD38. Therefore, in combination with the lack of a competent immune system, this strain of mice is not an ideal species for evaluating the off-target toxicity of the intact humanized biologics. The MM.1S IV mouse model, while representative of the quiescent progression of MM, may not be reflective of the aggressive cancer associated with RRMM patients. This may have resulted in significant single-dose activity of DARA monotherapy in MM.1S IV mice, a model not necessarily reflective of patients resistant to DARA therapy.

In aims 1 and 2, single time point images were used for evaluation of treated and untreated groups as well as biodistribution. This was done to reduce the complexity inherent in longitudinal, NIR fluorescence imaging of diffuse nature of MM intramedullar tumors. However, due to clonal and spatiotemporal heterogeneity in intra- and inter- patient levels, the comparison of these two groups may lose relevant information regarding changes in expression during disease progression. Longitudinal imaging of the DARA conjugates in both aims would allow for calculating pharmacokinetic parameters such as blood half-life to better determine dose response strategies and non-specific toxicities of the ADC. Use of longitudinal imaging would be especially useful in aim 1 using the preclinical MM models described previously to monitor spatiotemporal expression of CD38 during DARA therapy in more resistant MM cell lines.

Finally, this thesis only focused on evaluation of a single combination of linker and drug payload. Different linkers and drug payloads have their own unique mechanisms of action and can significantly affect DARs, hydrophobicity and biologic activity of the native DARA. Future studies should address this limitation by screening clinically relevant drug-linker combinations to identify the ideal DARA-based ADC for increasing the translatability of this thesis.

4.3 Future Work

As with the limitations, aim-specific future studies were addressed in each chapter. In brief, there are some general future studies that could be performed to improve upon the results and conclusions generated by each aim.

Evaluating binding and cytotoxicity of both DARA constructs in humanized, immunocompetent mouse models with spontaneous disease (i.e. vk*myc) are warranted. Immunocompromised and immunocompetent mice implanted with xenograft MM tumor cells resistant to frontline therapies (i.e. MM.1R) or expressing variable CD38 expression (i.e. U266) are also needed to truly recapitulate the BM microenvironment of RRMM patients. Use of multiple cell lines in an immunocompetent setting can also approximate different MM pathogenic behaviors for assessing the robustness of CD38 in the presence of heterogeneous protein expression and growth profiles. One important addition to the intramedullary model would be to test intramedullary imaging on focal lesions, *via* direct injection of cells into the long bone, since MM patients typically have a combination of diffuse and focal BM lesions.

With most ADCs in preclinical and clinical development relying on delivery of cytotoxic payloads such as maytansinoids or auristatins, the non-specific toxicities associated with such ADCs have also caused several to fail in the clinic. Therefore, other classes of payloads such as anti-inflammatory steroids are being explored for improved synergy between the antibody and contributing to overall anti-tumor immunity. Similarly with the drug payload, there is significant interest in linker chemistry to generate more homogeneous ADCs with consistent DARs without significant impact to the native antibody. New linkers and conjugation chemistries should also be explored to determine if Fc effector functions, such as ADCC and CDC, inherent to DARA can be performed even in the presence of a drug-linker complex. Evaluation of the concentration of

drug payload in plasma and non-tumor tissue and its toxicities on said tissues are warranted.

Finally, there is growing availability of tandem CT and NIR three-dimensional fluorescent systems that aim to utilize the functional imaging of NIR fluorescence with the high-resolution soft tissue contrast of CT. Our work has highlighted the use of NIR fluorescence in assessing changes to CD38 expression and evaluating novel biologics. Therefore, there is potential for using such dual-modal systems to generate co-registered results that can be used for early stratification of therapy response and identifying interactions of biologics with diffuse and focal bone lesions inherent in MM.

4.4 Conclusions

In conclusion, this study demonstrated a novel CD38-based ADC for potentially improving therapy response in RRMM patients. We took an integrated approach using NIR fluorescence to assess the mechanism of action and biodistribution of the native antibody and the ADC. We reasoned that the imaging techniques in this thesis can be utilized for efficient development of other contrast agents and therapeutics in preclinical MM models that have clinical translation potential.

4.5 References

1. Alexander DD, Mink PJ, Adami HO, et al (2007) Multiple myeloma: A review of the epidemiologic literature. Int J Cancer 120:40–61
2. Usmani S, Ahmadi T, Ng Y, et al (2016) Analysis of Real-World Data on Overall Survival in Multiple Myeloma Patients With ≥3 Prior Lines of Therapy Including a Proteasome Inhibitor (PI) and an Immunomodulatory Drug (IMiD), or Double Refractory to a PI and an IMiD. Oncologist 21:1355–1361
3. Bianchi G, Ghobrial IM (2013) Molecular mechanisms of effectiveness of novel therapies in multiple myeloma. Leuk Lymphoma 54:229–241
4. Fairfield H, Falank C, Avery L, Reagan MR (2016) Multiple myeloma in the marrow: Pathogenesis and treatments. Ann N Y Acad Sci 1364:32–51
5. Lonial S, Mitsiades CS, Richardson PG (2011) Treatment options for relapsed and refractory multiple myeloma. Clin Cancer Res 17:1264–1277
6. Liu Q, Kriksunov IA, Graeff R, et al (2005) Crystal structure of human CD38 extracellular domain. Structure 13:1331–1339
7. Czura AW, Czura CJ (2007) CD38 and CD157 : Biological Observations to Clinical Therapeutic Targets. Mol Med Rep 12:309–311
8. Ausiello CM, La Sala A, Ramoni C, et al (1996) Secretion of IFN-γ, IL-6, granulocyte-macrophage colony-stimulating factor and IL-10 cytokines after activation of human purified T lymphocytes upon CD38 ligation. Cell Immunol 173:192–197
9. Atanackovic D, Steinbach M, Radhakrishnan SV, Luetkens T (2016) Immunotherapies targeting CD38 in Multiple Myeloma. Oncoimmunology 5:1–11
10. Inoue S, Kontani K, Tsujimoto N, et al (1997) Protein-tyrosine phosphorylation by IgG1 subclass CD38 monoclonal antibodies is mediated through stimulation of the FcgammaII receptors in human myeloid cell lines. J Immunol 159:5226–32
11. Deaglio S, Vaisitti T, Billington R, et al (2007) CD38/CD19: A lipid raft-dependent signaling complex in human B cells. Blood 109:5390–5398
12. Brown DA (2013) Lipid Rafts. Encycl Biol Chem Second Ed 44:741–744
13. van de Donk NWCJ, Janmaat ML, Mutis T, et al (2016) Monoclonal antibodies targeting CD38 in hematological malignancies and beyond. Immunol Rev 270:95–112
14. Van De Donk NWCJ, Richardson PG, Malavasi F (2018) CD38 antibodies in multiple myeloma: Back to the future. Blood 131:13–29
15. Van De Donk NWCJ, Moreau P, Plesner T, et al (2016) Clinical efficacy and management of monoclonal antibodies targeting CD38 and SLAMF7 in multiple myeloma. Blood 127:681–695
16. Krejcik J, Casneuf T, Nijhof IS, et al (2016) Daratumumab depletes CD38+ immune regulatory cells, promotes T-cell expansion, and skews T-cell repertoire in multiple myeloma. Blood 128:384–394
17. Raimondo F Di (2018) Daratumumab for the Treatment of Multiple Myeloma. Front Immunol 9:
18. Ghose J, Viola D, Terrazas C, et al (2018) Daratumumab induces CD38 internalization and

impairs myeloma cell adhesion. Oncoimmunology 7:1–11

19. Lokhorst HM, Plesner T, Laubach JP, et al (2015) Targeting CD38 with Daratumumab Monotherapy in Multiple Myeloma. N Engl J Med 373:1207–1219

20. Usmani SZ, Nahi H, Plesner T, et al (2020) Daratumumab monotherapy in patients with heavily pretreated relapsed or refractory multiple myeloma: final results from the phase 2 GEN501 and SIRIUS trials. Lancet Haematol 7:e447–e455

21. Casneuf T, Xu XS, Adams HC, et al (2017) Effects of daratumumab on natural killer cells and impact on clinical outcomes in relapsed or refractory multiple myeloma. Blood Adv 1:2105–2114

22. Syed K, Nijhof IS, van Velzen J, et al (2016) CD38 expression and complement inhibitors affect response and resistance to daratumumab therapy in myeloma. Blood 128:959–970

23. Saltarella I, Desantis V, Melaccio A, et al (2020) Mechanisms of Resistance to Anti-CD38 Daratumumab in Multiple Myeloma. Cells 9:1–14

24. Van De Donk NWCJ, Usmani SZ (2018) CD38 antibodies in multiple myeloma: Mechanisms of action and modes of resistance. Front Immunol 9:1–12

25. Chillemi A, Quarona V, Zito A, et al (2015) Generation and Characterization of Microvesicles after Daratumumab Interaction with Myeloma Cells. Blood 126:1849–1849

26. Morandi F, Marimpietri D, Horenstein AL, et al (2018) Microvesicles released from multiple myeloma cells are equipped with ectoenzymes belonging to canonical and non-canonical adenosinergic pathways and produce adenosine from ATP and NAD+. Oncoimmunology 7:

27. Neri P, Maity R, Tagoug I, et al (2017) Single Cell Resolution Profiling Defines the Innate and Adaptive Immune Repertoires Modulated By Daratumumab and IMiDs Treatment in Multiple Myeloma (MM). Blood 130:123–123

28. Viola D, Dona A, Gunes EG, et al (2018) Immune Mediated Mechanisms of Resistance to Daratumumab. Blood 132:3201–3201

29. Plesner T, Arkenau HT, Gimsing P, et al (2016) Phase 1/2 study of daratumumab, lenalidomide, and dexamethasone for relapsed multiple myeloma. Blood 128:1821–1828

30. Palumbo A, Chanan-Khan A, Weisel K, et al (2016) Daratumumab, bortezomib, and dexamethasone for multiple myeloma. N Engl J Med 375:754–766

31. Nijhof IS, Groen RWJ, Noort WA, et al (2015) Preclinical evidence for the therapeutic potential of CD38-Targeted Immuno-chemotherapy in multiple Myeloma patients refractory to Lenalidomide and Bortezomib. Clin Cancer Res 21:2802–2810

32. Nijhof IS, Van Bueren JJL, Van Kessel B, et al (2015) Daratumumab-Mediated lysis of primary multiple myeloma cells is enhanced in combination with the human Anti-KIR antibody IPH2102 and lenalidomide. Haematologica 100:263–268

33. Nooka AK, Joseph NS, Kaufman JL, et al (2019) Clinical efficacy of daratumumab, pomalidomide, and dexamethasone in patients with relapsed or refractory myeloma: Utility of re-treatment with daratumumab among refractory patients. Cancer 1–10

34. Lu J, Jiang F, Lu A, Zhang G (2016) Linkers having a crucial role in antibody–drug conjugates. Int J Mol Sci 17:

35. Jain N, Smith SW, Ghone S, Tomczuk B (2015) Current ADC Linker Chemistry. Pharm Res

32:3526–3540

36. Bhakta S (et al. . (2013) Antibody Drug Conjugates - Methods in Molecular Biology

37. Nejadmoghaddam M-R, Minai-Tehrani A, Ghahremanzadeh R, et al (2019) Antibody-Drug Conjugates: Possibilities and Challenges. Avicenna J Med Biotechnol 11:3–23

38. Yu B, Liu D (2019) Antibody-drug conjugates in clinical trials for lymphoid malignancies and multiple myeloma. J Hematol Oncol 12:1–17

39. Grobmyer S R;, Moudgil B M; (2010) Cancer Nanotechnology: Methods and Protocols

40. Chen H, Lin Z, Arnst KE, et al (2017) Tubulin inhibitor-based antibody-drug conjugates for cancer therapy. Molecules 22:

41. Mandelbaum-Shavit F, Wolpert-DeFilippes MK, Johns DG (1976) Binding of maytansine to rat brain tubulin. Biochem Biophys Res Commun 72:40–46

42. Rai SS, Wolff J (1996) Localization of the vinblastine-binding site on β-tubulin. J Biol Chem 271:14707–14711

43. Ravry MJR, Omura GA, Birch R (1985) Phase II evaluation of maytansine (NSC 153858) in advanced cancer. Am J Clin Oncol 8:148–150

44. Cassady JM, Chan KK, Floss HG, Leistner E (2004) Recent developments in the maytansinoid antitumor agents. Chem Pharm Bull 52:1–26

45. Donaghy H (2016) Effects of antibody, drug and linker on the preclinical and clinical toxicities of antibody-drug conjugates. MAbs 8:659–671

46. Hunter FW, Barker HR, Lipert B, et al (2020) Mechanisms of resistance to trastuzumab emtansine (T-DM1) in HER2-positive breast cancer. Br J Cancer 122:603–612

47. Erickson HK, Lambert JM (2012) ADME of antibody-maytansinoid conjugates. AAPS J 14:799–805

48. Kashiwagi S, Brauns T, Gelfand J, et al (2014) Laser vaccine adjuvants Laser vaccine adjuvants. 5515:

49. Miao Z, Ren G, Liu H, et al (2010) Cy5.5-labeled Affibody molecule for near-infrared fluorescent optical imaging of epidermal growth factor receptor positive tumors. J Biomed Opt 15:036007

50. Gong H, Kovar JL, Cheung L, et al (2014) A comparative study of affibody, panitumumab, and EGF for near-infrared fluorescence imaging of EGFR- and EGFRvIII-expressing tumors. Cancer Biol Ther 15:185–193

51. Gong H, Little G, Chen H, et al (2015) In Vivo Imaging of Xenograft Tumors Using an Epidermal Growth Factor Receptor-Specific Affibody Molecule Labeled with a Near-infrared Fluorophore. Neoplasia 12:139-IN9

52. Samkoe KS, Gunn JR, Marra K, et al (2017) Toxicity and Pharmacokinetic Profile for Single-Dose Injection of ABY-029: a Fluorescent Anti-EGFR Synthetic Affibody Molecule for Human Use. Mol Imaging Biol 19:512–521

53. Hage C, Gremse F, Griessinger CM, et al (2018) Comparison of the accuracy of FMT/CT and PET/MRI for the assessment of antibody biodistribution in squamous cell carcinoma xenografts

54. Tsumura R, Sato R, Furuya F, et al (2015) Feasibility study of the Fab fragment of a monoclonal

antibody against tissue factor as a diagnostic tool. Int J Oncol 47:2107–2114

55. Peterson NC, Wilson GG, Huang Q, et al (2016) Biodistribution analyses of a near-infrared, fluorescently labeled, bispecific monoclonal antibody using optical imaging. Comp Med 66:90–99

56. Wang Y, Liu L, Fan S, et al (2020) Antibody-drug conjugate using ionized CYS-linker-mmae as the potent payload shows optimal therapeutic safety. Cancers (Basel) 12:

57. Kulkarni C, Finley JE, Bessire AJ, et al (2017) Development of Fluorophore-Labeled Thailanstatin Antibody-Drug Conjugates for Cellular Trafficking Studies. Bioconjug Chem 28:1041–1047

58. Giddabasappa A, Gupta VR, Norberg R, et al (2016) Biodistribution and targeting of anti-5t4 antibody-drug conjugate using fluorescence molecular tomography. Mol Cancer Ther 15:2530–2540

59. Knutson S, Raja E, Bomgarden R, et al (2016) Development and evaluation of a fluorescent antibody-drug conjugate for molecular imaging and targeted therapy of pancreatic cancer. PLoS One 11:1–25

60. Bhattacharyya S, Patel NL, Wei L, et al (2014) Synthesis and biological evaluation of panitumumab-IRDye800 conjugate as a fluorescence imaging probe for EGFR-expressing cancers. Medchemcomm 5:1337–1346

61. Zhou Q, Vega Leonel JCM, Santoso MR, et al (2021) Molecular imaging of a fluorescent antibody against epidermal growth factor receptor detects high-grade glioma. Sci Rep 11:1–13

62. Paudyal B, Paudyal P, Shah D, et al (2014) Detection of vascular endothelial growth factor in colon cancer xenografts using bevacizumab based near infrared fluorophore conjugate. J Biomed Sci 21:

63. Sampath L, Kwon S, Ke S, et al (2007) Dual-labeled trastuzumab-based imaging agent for the detection of human epidermal growth factor receptor 2 overexpression in breast cancer. J Nucl Med 48:1501–1510

64. Gao RW, Kaplan MJ, Rosenthal EL, et al (2018) Safety of panitumumab-IRDye800CW and cetuximab-IRDye800CW for fluorescence-guided surgical navigation in head and neck cancers. Theranostics 8:2488–2495

65. Rosenthal EL, Warram JM, De Boer E, et al (2015) Safety and tumor specificity of cetuximab-IRDye800 for surgical navigation in head and neck cancer. Clin Cancer Res 21:3658–3666

66. Heath CH, Deep NL, Sweeny L, et al (2012) Use of panitumumab-IRDye800 to image microscopic head and neck cancer in an orthotopic surgical model. Ann Surg Oncol 19:3879–3887

67. Marshall M V., Draney D, Sevick-Muraca EM, Olive DM (2010) Single-dose intravenous toxicity study of IRDye 800CW in sprague-dawley Rats. Mol Imaging Biol 12:583–594

68. Cho N, Shokeen M (2019) Changing Landscape of Optical Imaging in Skeletal Metastases. J Bone Oncol 17:100249

69. Withana NP, Blum G, Sameni M, et al (2012) Cathepsin B inhibition limits bone metastasis in breast cancer. Cancer Res 72:1199–1209

70. Kozloff KM, Quinti L, Patntirapong S, et al (2009) Non-invasive optical detection of cathepsin K-mediated fluorescence reveals osteoclast activity in vitro and in vivo. Bone 44:190–198

71. Runnels JM, Carlson AL, Pitsillides C, et al (2011) Optical techniques for tracking multiple

myeloma engraftment, growth, and response to therapy. J Biomed Opt 16:011006

72. Jia X, Roccaro AM, Azab AK, et al (2009) CXCR4 inhibitor AMD3100 disrupts the interaction of multiple myeloma cells with the bone marrow microenvironment and enhances their sensitivity to therapy. Blood 113:4341–4351

73. Shishido S, Bonig H, Kim Y-M (2014) Role of Integrin Alpha4 in Drug Resistance of Leukemia. Front Oncol 4:99

74. Peng L, Liu R, Marik J, et al (2006) Combinatorial chemistry identifies high-affinity peptidomimetics against α4β1 integrin for in vivo tumor imaging. Nat Chem Biol 2:381–389

75. Lam KS, Liu R, Xiao W, et al (2008) In vivo optical imaging of human lymphoma xenograft using a library-derived peptidomimetic against 4 1 integrin. Mol Cancer Ther 7:432–437

76. Bruins WSC, Zweegman S, Mutis T, van de Donk NWCJ (2020) Targeted Therapy With Immunoconjugates for Multiple Myeloma. Front Immunol 11:

77. Cho N, Ko S, Shokeen M (2020) Preclinical Development of Near-Infrared-Labeled CD38-Targeted Daratumumab for Optical Imaging of CD38 in Multiple Myeloma. Mol Imaging Biol 186–195

78. Hogan KA, Chini CCS, Chini EN (2019) The Multi-faceted Ecto-enzyme CD38: Roles in immunomodulation, cancer, aging, and metabolic diseases. Front Immunol 10:1–12

79. Malavasi F, Deaglio S, Damle R, et al (2011) CD38 and chronic lymphocytic leukemia: A decade later. Blood 118:3470–3478

80. Martin TG, Corzo K, Chiron M, et al (2019) Therapeutic Opportunities with Pharmacological Inhibition of CD38 with Isatuximab. Cells 8:1522

81. Moreno L, Perez C, Zabaleta A, et al (2019) The mechanism of action of the anti-CD38 monoclonal antibody isatuximab in multiple myeloma. Clin Cancer Res 25:3176–3187

82. Nijhof IS, Groen RWJ, Lokhorst HM, et al (2015) Upregulation of CD38 expression on multiple myeloma cells by all-trans retinoic acid improves the efficacy of daratumumab. Leukemia 29:2039–2049

83. Warram JM, de Boer E, Sorace AG, et al (2014) Antibody-based imaging strategies for cancer. Cancer Metastasis Rev 33:809–22

84. Ghai A, Maji D, Cho N, et al (2018) Preclinical Development of CD38-Targeted [89 Zr]Zr-DFO-Daratumumab for Imaging Multiple Myeloma . J Nucl Med 59:216–222

85. Moses WW (2011) Fundamental limits of spatial resolution in PET. Nucl Instruments Methods Phys Res Sect A Accel Spectrometers, Detect Assoc Equip 648:S236–S240

86. Smith AM, Mancini MC, Nie S (2009) Bioimaging: Second window for in vivo imaging. Nat Nanotechnol 4:710–711

87. Oliveira S, Cohen R, van Walsum MS, et al (2012) A novel method to quantify IRDye800CW fluorescent antibody probes ex vivo in tissue distribution studies. EJNMMI Res 2:1–9

88. Zhang K (2008) Center for Drug Evaluation and Pharmacology Review (S): Olopatadine NDA21861. Pharmacol NDA Rev Eval 1–214

89. Oyajobi BO, Muñoz S, Kakonen R, et al (2007) Detection of myeloma in skeleton of mice by

whole-body optical fluorescence imaging. Mol Cancer Ther 6:1701–1708

90. Ma T, Sun X, Cui L, et al (2014) Molecular imaging reveals trastuzumab-induced epidermal growth factor receptor downregulation in vivo. J Nucl Med 55:1002–1007

91. Liu Z, Sun X, Liu H, et al (2014) Early assessment of tumor response to gefitinib treatment by noninvasive optical imaging of tumor vascular endothelial growth factor expression in animal models. J Nucl Med 55:818–823

92. Ryman JT, Meibohm B (2017) Pharmacokinetics of monoclonal antibodies. CPT Pharmacometrics Syst Pharmacol 6:576–588

93. Eigenmann MJ, Fronton L, Grimm HP, et al (2017) Quantification of IgG monoclonal antibody clearance in tissues. MAbs 9:1007–1015

94. Paton-Hough J, Chantry AD, Lawson MA (2015) A review of current murine models of multiple myeloma used to assess the efficacy of therapeutic agents on tumour growth and bone disease. Bone 77:57–68

95. Lonial S, Durie B, Palumbo A, San-Miguel J (2016) Monoclonal antibodies in the treatment of multiple myeloma: Current status and future perspectives. Leukemia 30:526–535

96. Pick M, Vainstein V, Goldschmidt N, et al (2018) Daratumumab resistance is frequent in advanced-stage multiple myeloma patients irrespective of CD38 expression and is related to dismal prognosis. Eur J Haematol 100:494–501

97. Gandhi UH, Cornell RF, Lakshman A, et al (2019) Outcomes of patients with multiple myeloma refractory to CD38-targeted monoclonal antibody therapy. Leukemia 33:2266–2275

98. Krejcik J, Frerichs KA, Nijhof IS, et al (2017) Monocytes and granulocytes reduce CD38 expression levels on myeloma cells in patients treated with daratumumab. Clin Cancer Res 23:7498–7511

99. Sanchez L, Dardac A, Madduri D, et al (2021) B-cell maturation antigen (BCMA) in multiple myeloma: the new frontier of targeted therapies. Ther Adv Hematol 12:204062072198958

100. Ailawadhi S, Kelly KR, Vescio RA, et al (2019) A Phase I Study to Assess the Safety and Pharmacokinetics of Single-agent Lorvotuzumab Mertansine (IMGN901) in Patients with Relapsed and/or Refractory CD–56-positive Multiple Myeloma. Clin Lymphoma, Myeloma Leuk 19:29–34

101. Chalouni C, Doll S (2018) Fate of Antibody-Drug Conjugates in Cancer Cells. 1–12

102. Tassone P, Gozzini A, Goldmacher V, et al (2004) In vitro and in vivo activity of the maytansinoid immunoconjugate huN901-N2′-deacetyl-N2′-(3-mercapto-1- oxopropyl)-maytansine against CD56+ multiple myeloma cells. Cancer Res 64:4629–4636

103. Zhang X, Zhang C, Yang X, et al (2019) Design, synthesis and evaluation of anti-CD38 antibody drug conjugate based on Daratumumab and maytansinoid. Bioorganic Med Chem 27:479–482

104. Dawicki W, Allen KJH, Jiao R, et al (2019) Daratumumab- 225 Actinium conjugate demonstrates greatly enhanced antitumor activity against experimental multiple myeloma tumors. Oncoimmunology 8:1–9

105. Cilliers C, Nessler I, Christodolu N, Thurber GM (2017) Tracking Antibody Distribution with Near-Infrared Fluorescent Dyes: Impact of Dye Structure and Degree of Labeling on Plasma Clearance. Mol Pharm 14:1623–1633

106. Bailey AO, Houel S, Scheffler K, et al (2017) Complete characterization of a lysine-linked antibody drug conjugate by native LC / MS intact mass analysis and peptide mapping. Appl Note 72511

107. Kurdi AT, Glavey S V., Bezman NA, et al (2018) Antibody-Dependent Cellular Phagocytosis by Macrophages is a Novel Mechanism of Action of Elotuzumab. Mol Cancer Ther 17:1454–1463

108. Olson B, Li Y, Lin Y, et al (2018) Mouse Models for Cancer Immunotherapy Research. Cancer Discov 8:1358–1365

109. Boswell CA, Tesar DB, Mukhyala K, et al (2010) Effects of charge on antibody tissue distribution and pharmacokinetics. Bioconjug Chem 21:2153–2163

110. Boswell CA, Mundo EE, Zhang C, et al (2011) Impact of drug conjugation on pharmacokinetics and tissue distribution of Anti-STEAP1 antibody-drug conjugates in rats. Bioconjug Chem 22:1994–2004